geosciences

MDPI

*Review*

# Influence of Surface Roughness and Particle Characteristics on Soil–Structure Interactions: A State-of-the-Art Review

**Runshen Wang [1,2,*], Dominic E. L. Ong [1,2], Mohammud I. Peerun [1,2] and Dong-Sheng Jeng [3]**

[1] School of Engineering and Built Environment, Griffith University, Nathan 4111, Australia; d.ong@griffith.edu.au (D.E.L.O.); irfaan.peerun@griffithuni.edu.au (M.I.P.)
[2] Cities Research Institute, Griffith University, Southport 4215, Australia
[3] School of Engineering and Built Environment, Griffith University, Gold Coast Campus, Southport 4222, Australia; d.jeng@griffith.edu.au
* Correspondence: jason.wang2@griffithuni.edu.au

**Abstract:** The study of soil–structure interface behavior contributes to the fundamental understanding of engineering performance and foundation design optimization. Previous research studies the effect of soil characteristics and surface roughness property on the soil–material interface mechanism via interface shear test. The reviews utilizing past established laboratory studies and more recent tests based on state-of-the-art technologies reveal that surface roughness significantly affects interface shear performances in the studies of soil–structure interactions, especially in peak shear strength development. A preliminary but original investigative study by the authors was also carried out using a sophisticated portable surface roughness gauge to define the material surface roughness properties in order to study the interface behavior parametrically. Additionally, using the authors' own original research findings as a proof-of-concept innovation, particle image velocimetry (PIV) technology is applied using a digital single-lens reflex (DSLR) camera to capture sequential images of particle interactions in a custom-built transparent shear box, which validate the well-established four-stage soil shearing model. The authors also envisaged that machine learning, e.g., artificial neural network (ANN) and Bayesian inference method, amongst others, as well as numerical modeling, e.g., discrete element method (DEM), have the potential to also promote research advances on interface shear mechanisms, which will assist in developing a greater understanding in the complex study of soil–structure interactions.

**Keywords:** interface shear test; surface roughness; critical roughness; random or ribbed surface roughness; friction development; PIV technology



**Citation:** Wang, R.; Ong, D.E.L.; Peerun, M.I.; Jeng, D.-S. Influence of Surface Roughness and Particle Characteristics on Soil–Structure Interactions: A State-of-the-Art Review. *Geosciences* **2022**, *12*, 145. https://doi.org/10.3390/geosciences12040145

Academic Editors: Mohamed Shahin and Jesus Martinez-Frias

Received: 17 January 2022
Accepted: 17 March 2022
Published: 23 March 2022



## 1. Introduction

Soil–structure interfaces play key roles in transferring construction gravity and external loads from the substructures to the ground. The research on soil–structure interface mechanism and behavior is critical for geotechnical engineering applications. In recent years, advancements in technology have influenced how designs are conceptualized, considering sustainability aspects [1–4], challenges faced in laboratory soil tests [5,6], soil–structure simulations [7,8], and inferior in situ geomaterial conditions requiring biological [9–14] or chemical stabilization [15–17]. For instance, the study of the effects of the interface on soil–structure interactions have benefitted from this technological advancement to include the design of deep foundations [18–23], pavement–subgrade behavior [24,25], tunneling [26–33], mechanically stabilized geogrid retaining walls, and ground improvement in soft soils [34–36]. For example, in the design of deep foundations, static and dynamic pile load tests provide the necessary evidence-based field observational results to verify the accuracy and reliability of the initially adopted pile design parameters. Previous research conducted via the conventional static load tests evidenced that the designed pile shaft capacities in many projects had been grossly over-designed due to the lack of reliable pile–soil

interface parameters [37,38]. As a result, it is not uncommon that the construction costs of deep foundations often account for 20–25% of the total costs of the project [37], which is economically unsustainable. Thus, understanding the soil–structure interface mechanism can help contribute to potentially greater savings in the design of pile foundations. In another example, it has been shown that installing underground sewers via the pipe jacking method would induce varying jacking forces according to the traversed geological layers during jacking operations [28,30,39]. Pipe jacking forces that are over-predicted will result in pipe wall fractures or excessive ground heave, whereas under-predicted jacking forces will prevent the micro-tunneling boring machine (MTBM) from breaking through the receiving shaft or cause the collapse of the tunnel face excavation, leading to ground loss [40]. As such, it is evident that the influence of surface roughness not only contributes to the economics of underground construction, but also seeks to enhance construction safety.

The research carried out on the influence of surface roughness is often closely associated with the understanding of particle characteristics as well. Normally, such studies are conducted via the conventional shear tests and interface shear tests. Based on conventional shear test results, Coulomb (1773) defined a linear failure envelope for soil limit states and found that fully developed shear resistance results in shear failure [41]. The fully developed shear resistance, also known as soil shear strength, has been determined using laboratory and field tests. Even though soil characteristics obtained from conventional shear tests may be used to broadly predict general soil–structure behavior of localized geostructures (e.g., retaining wall in the plane-strain direction), some engineering applications involving linear infrastructure, such as tunneling, pipe jacking, and pavement–subgrade interactions, would require greater accuracy due to the often varying geological profiles in the plane-stress (horizontal) direction. For example, Staheli (2006) conducted interface direct shear tests using granular materials and various pipe materials with varying surface roughness to analyze pipe jacking forces [42]. Based on the test results, the frictional jacking force model was established for granular materials, but it was only applicable to unlubricated jacking drives, hence the obvious limitation of the research to mimic real-life phenomena. Even though surface roughness [43,44] has significant influences on the interface shear mechanisms, other interface characteristics, such as surface hardness [45], particle angularity [46,47], mean particle size [48], particle breakage [49], and confinement condition [50,51], have also been found to affect the soil's shear behavior [28,29,52,53]. Peerun et al. (2020) successfully conducted direct shear tests on reconstituted rock spoil from various geological lithologies to develop a mathematical model to reliably determine the often-elusive effective jacking forces to propel MTBM forward in a typical tunneling project [30]. Similarly, in the research of [54], the strength parameters of the reconstituted rock spoil were determined and then integrated into the jacking force model using direct shear tests to provide an accurate jacking force prediction. From the discussions above, it is clear that the development of friction is complex, as it involves many other parameters that are difficult to quantify for consistent use in design.

Therefore, in this review paper, conventional shear tests, such as the (i) direct shear test, (ii) simple shear test, and (iii) ring shear test, are carefully reviewed in terms of their operating procedures, advantages, and disadvantages to study soil shear strength. This is then followed by the review of the critical factors, such as (i) surface roughness, (ii) particle angularity, (iii) mean particle size, (iv) surface hardness, (v) particle breakability, and (vi) confinement condition, that influence the complex behavior of soil–material interfaces in soil–structure interaction problems. Due to the historical challenges in observing and describing the microscopic-level interface interactions, a proof-of-concept innovative transparent Perspex shear box has been designed, fabricated, and commissioned by the authors to help with the visualization process, with preliminary results discussed. In tandem, the effectiveness of integrating the shear testing with technologically advanced visualization tools, such as (i) particle image velocimetry (PIV) and (ii) discrete element modeling (DEM), is reviewed and investigated. Finally, the potential use of machine learning techniques,

such as (i) artificial neural network (ANN) and (ii) Bayesian updating process, are discussed with respect to practical engineering soil–material interface applications.

This review paper develops the understanding of soil–structure interactions due to surface roughness and particle characteristics. Understanding and results derived from past research, as well as the authors' own original results using the direct shear test (DST) method, are presented and discussed in detail. Particle image velocimetry (PIV) technology is the main analytical tool championed by the authors and has also been integrated into this review paper as a means for verification to increase the confidence levels of the results presented herein. Furthermore, other supplementary methods to enhance the understanding of soil–structure interactions are also briefly introduced, such as neural network, DEM, 3D printing, and Bayesian method.

## 2. Conventional Shear Tests

Conventional shear tests that will be discussed in this paper are (i) direct shear test, (ii) simple shear test, and (iii) ring shear test, which measure the soil shear strength.

### 2.1. Direct Shear Test

Direct shear tests (Figure 1) are simple to conduct and have typically been used for site investigation and foundation design. It has been widely used for shear strength characteristics of granular material. Additionally, the soil sample is prepared with a small thickness, which allows the pore water pressure to dissipate rapidly. The shear box is sheared along the predetermined failure plane, with constant tangential shear force or displacement while applying a normal force on the sample [55]. While the peak shear strength and residual strength are measured by S-type load cell, vertical and horizontal displacement are recorded by linear variable differential transformers (LVDTs) (see Figure 2). Based on a linear graph of shear stress against normal stress, the slope and the intercept value represent soil friction angle and cohesion stress. The equipment setup and test procedures of the direct shear test are fully detailed in ASTM D3080 and AS1289.


**Figure 1.** Direct shear test apparatus (HM-382F) produced by Gilson company. This original direct shear apparatus has since been modified by the authors for use as an interface shear apparatus.

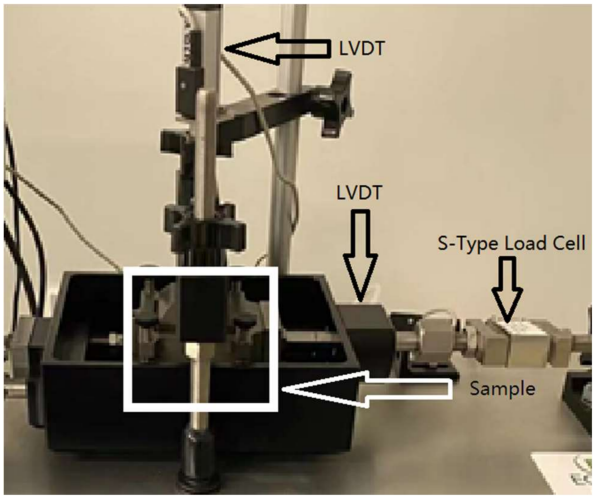


**Figure 2.** DST apparatus used in this research.

There are three kinds of DST methods: the slow shear test (or S-test), quick shear test (or Q-test, with the speed of 0.02 mm/min), and consolidated quick shear test. The Chinese standard [56,57] recommends the quick shear test for site investigation and requires that each soil type be tested at least four times. The specimen of DST is confined by a rectangular or circular metal shear box, usually circular, with 61.8-mm-diameter width and 20-mm height. Australian standards recommend slow shearing tests for peak shear strength and residual shear strength. The procedures of direct shear tests are shown below in Federal Highway Administration (FHWA) and AS 1289 6.22 [56]:

1. Place the top half of the shear box on the bottom one with two clamping screws fixed, as shown in Figure 3.
2. Fix the retaining plate and the perforated grid plate, and the shearing force is perpendicular to a serration orientation of the plate.
3. Fix the perforated grid plate and the loading pad on top, and then place the assembly into the water chamber; slot the end onto the pushrod.
4. Fix the horizontal and vertical LVDTs on the specific location.
5. Apply normal stress and wait for consolidation to be completed (cohesionless soil is consolidated instantaneously).
6. Shear the soil specimen with the constant rate ($R_d$), which is determined by the sample's hydraulic conductivity, and the formula is shown below [58].

$$R_d = \frac{d_f}{t_f} \quad (1)$$

where:

$t_f$—estimated elapsed time to specimen failure in shearing apparatus;
$t_{50}$—consolidation with 50 percent under the maximum normal stress;
$t_{90}$—consolidation with 90 percent under the maximum normal stress;
$d_f$—estimated relative lateral displacement at failure, $d_f = 10$ mm (for overconsolidated fine-grained soil), otherwise $d_f = 5$ mm.

Note: if the normal deformation versus logarithmic time is significant yield, $t_f = 50t_{50}$, otherwise, $t_f = 11.6t_{90}$. Due to the absence of soil consolidation data in the specific case, Section 9.10.3 of ASTM D3080 also provides a table for a minimum time to failure (Table 1).

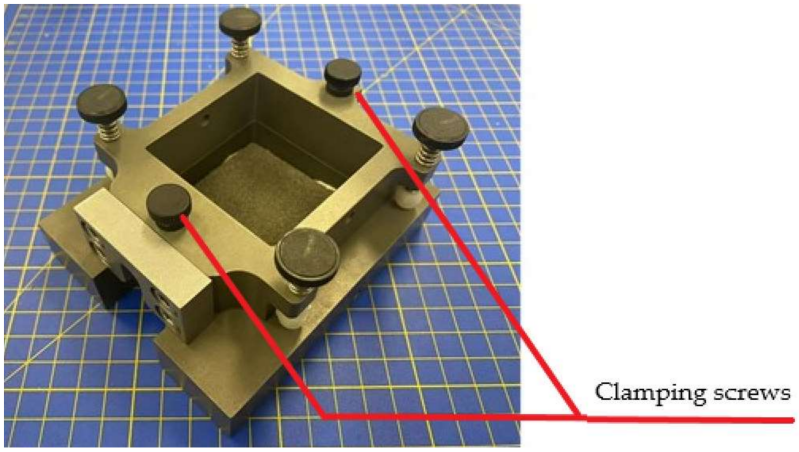


**Figure 3.** Typical shear box.

**Table 1.** Minimum time to failure [58].

| USCS Classification (D2487) | Minimum Time to Failure, $t_f$ |
|---|---|
| SW, SP (<5% fines) | 10 min |
| SW-SM, SP_SM, SM (>5% fines) | 60 min |
| SC, ML, CL, SP-SC | 200 min |
| MH, CH | 24 h |

After several specimens are tested using the DST method, the peak shear strength and residual strength are obtained with different normal effective stresses. Then, according to Mohr–Coulomb constitutive relation, cohesion (c) and internal friction angle are determined by Equation (2).

$$S = c + \sigma \tan \varphi \quad (2)$$

where:

S—shearing strength of soil (kPa);
C—cohesion strength of soil (kPa);
σ—normal effective strength (kPa);
$\varphi$—internal friction angle (°).

The relative displacement of the top and bottom shear box along the predetermined failure plane reduces the shearing area. Thus, Yu et al. (2014) apply the modified method for direct shear test results, including the single-point area correction method and multipoint area correction method [59]. The single-point area correction method applies Newton's second law to determine the shear stress (see Equation (3)). For the strain-controlled shear test, the acceleration (a) is zero. Thus, Equation (3) is converted to Equation (4), which simply considers the effect of shear area reduction. On the other hand, the multipoint area correction method applies the principles of momentum and energy conservation (see Equations (5) and (6)). This method assumes the product of velocity variation in the initial state and mass is much lower than the time integral of horizontal load. Thus, Equations (5) and (6) are integrated into Equation (7).

Single-point area correction method:

$$F - \tau A = ma \quad (3)$$

$$\tau_f = \tau' = \frac{\tau A_0}{A_2} = \frac{CRA_0}{A_2} = \tau\beta \quad (4)$$

Multipoint area correction method:

$$\int_{t_2}^{t_1} [F(t)dt - \tau A(t)dt] = m\Delta v \quad (5)$$

$$\int_{s_2}^{s_1} [F(s)ds - \tau A(s)ds] = \Delta E \quad (6)$$

$$\tau = \frac{\int_{p_2}^{p_1} F(p)dp}{\int_{p_2}^{p_1} A(p)dp} \quad (7)$$

The results of a conventional direct shear test include the shear stress at peak and residual states, as well as volumetric deformation of the sample. Li and Aydin (2010) developed a four-stage shearing model based on direct shear test results and revealed that the process of direct shear tests could be divided into four stages: (1) end zone deformation: peak stress tends to concentrate at the shear zone's end, and the soil specimen is compressed until it reaches the lowest volumetric strain; (2) particle interlocking: this stage plays a major role in increasing volumetric strain until it reaches the peak shear stress; (3) shear zone formation: particles rearrange where smaller particles flow into the specimen void, and larger particles rotate; and (4) stable shear: there is no further compression or dilation at this stage, and the shear stress remains constant [60]. This four-stage model will subsequently be used to validate the preliminary tests carried out using the transparent shear box to verify its applicability to study the interaction between surface roughness and the in-contact material (soil) types.

### 2.2. Simple Shear Test

Bjerrum and Landva (1966) established the simple shear test, which is widely used to determine the constant volume strength and stress–strain relationship of cohesive soils [61,62]. Meanwhile, the understanding of the shear mechanism in simple shear tests contributes to solving the offshore gravity-based structure and slope stability problem [63]. Comparing soil specimen in the direct shear test, the soil specimen in the simple shear test is restricted by two parallel rigid platens, which maintain the cross-sectional area constantly. Thus, the failure mode of soil specimen in the simple shear is present not only in the horizontal predetermined failure plane, as well as direct shear tests, but exists along the vertical plane (see Figure 4). Due to the difference in shear mechanisms, direct shear tests provide a higher shearing strength and stiffness than simple shear tests [63].

According to ASTM D6528-17 requirements, the tested cohesive soil can be intact, laboratory reconstituted, and compacted soils [64]. The soil specimen is one-dimensionally consolidated until the excess pore water pressures are dissipated. Meanwhile, the pore water pressures remain constant during the simple shear test in the undrained condition. Thus, the variation in normal stress equals the variation in effective stress. However, reconstituted and compacted soil preparation is not detailed in the standard, thus limiting the study of soil–structure interactions in silty "sand-like" soils.

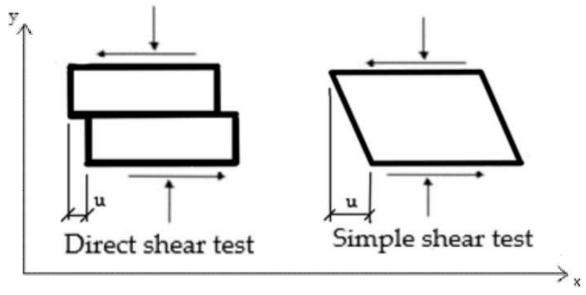


**Figure 4.** Schematic of direct shear test and simple shear test.

### 2.3. Ring Shear Test

The irreversible shearing direction of the ring direct shear test (see Figure 5) leads to large shear displacement, which contributes to the reorientation of the tested particles [65]. Thus, ring shear tests provide a more accurate residual shear strength than conventional direct shear tests and triaxial tests [66]. As there is no limitation on shearing displacement, the ring shear test has proven its reliability in the back analyses of landslides [67,68]. However, the low shearing rate of a ring shear test cannot be utilized to simulate "extremely rapid landslides" [66,69]. Meanwhile, the rubber edge of the ring shear apparatus causes an invisible area, which disrupts clear observations of the development of the shear band. The use of an opaque box makes particle image capture impossible and limits the application of state-of-the-art image processing techniques to develop an enhanced understanding of soil–structure interactions [66,70,71].

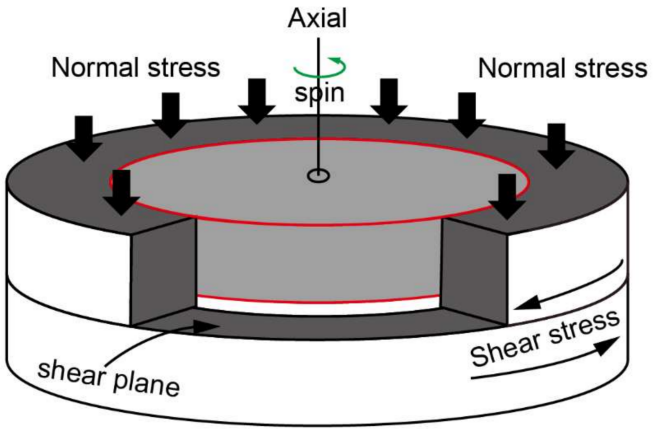


**Figure 5.** The principle of ring shear test.

## 3. Interface Shear Strength

The soil shear strength investigation contributes to the fundamental understanding of construction performance and deep foundation design. However, the research of soil–structure interface behavior cannot be simply limited to soil characteristics, but must also include surface roughness properties. Therefore, the interface shear test apparatus is manufactured based on conventional shear tests, including direct shear tests, simple shear tests, and ring shear tests. Potyondy (1961) first developed the research on soil–structure interface behavior and found that shear resistance is influenced by several characteristics, such as particle size distribution, soil moisture content, normal stress, structure material, and surface finish. As a result, the skin friction angle increases until the value of surface roughness reaches the soil internal friction angle. With advanced technology applied in interface shear tests, the current understanding reveals that several parameters affect the soil–structure interface behavior, including surface roughness [43,44], mean particle size [48], surface hardness [45], particle angularity [46,47], particle breakage [49], and confinement condition [50,51].

### 3.1. Influence of Surface Roughness

#### 3.1.1. Background

Potyondy (1961) first investigated the effect of surface roughness on soil–structure interface shear behavior, where surface roughness is simply described as "rough" or "smooth". Based on this research approach, subsequent research determined the 2D cross-sectional profile of the material surface (see Figure 6) and defined the surface roughness with a series of roughness parameters (see Table 2) and applied the theory to engineering applications [72,73]. Reference values of roughness parameters include the maximum height of the profile ($R_{zi}$ or $R_z$) and arithmetical mean height of the profile (or average roughness, $R_a$).

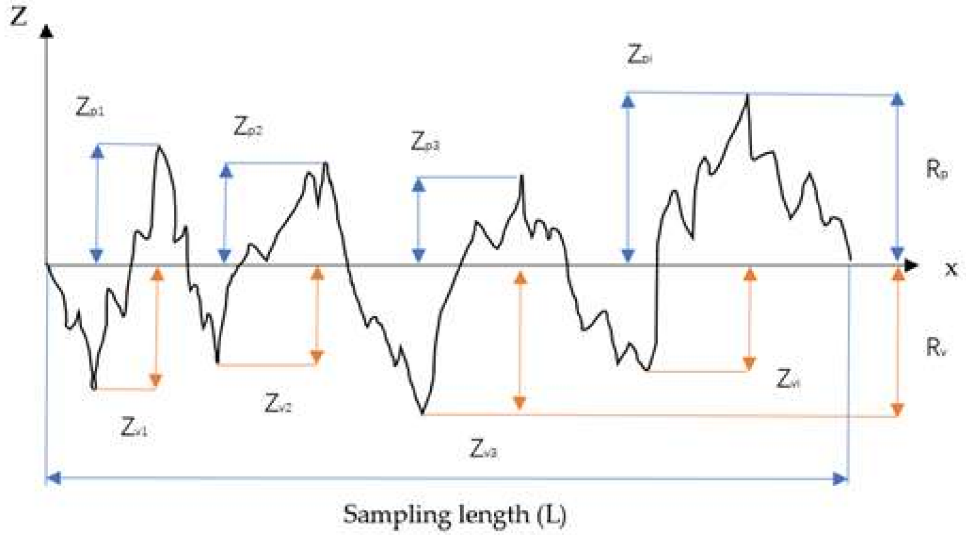


**Figure 6.** The maximum peak height and the maximum valley depth.

**Table 2.** Characteristics of surface roughness parameters.

| Parameters | Characteristics | Formula |
|---|---|---|
| $Z_{pi}$ | The ith peck height of the material roughness profile | - |
| $Z_{vi}$ | The ith valley depth of the material roughness profile | - |
| $R_{pi}$ | The maximum peak height of the material roughness profile within a sampling length (L or lr) | $R_{pi} = \max Z(x)$ |
| $R_{vi}$ | The maximum valley depth of the material roughness profile within a sampling length (L or lr) | $R_{vi} = \lvert\min Z(x)\rvert$ |
| $R_{zi}$ | The overall height of the roughness profile $R_{zi}$ is the sum of $R_{pi}$ and $R_{vi}$ within a sampling length (L or lr) | $R_{zi} = R_{pi} + R_{vi}$ |
| $R_{max}$ | Maximum $R_{zi}$ value over assessment length | - |
| $R_z$ | Average $R_{zi}$ value over assessment length | $R_z = \frac{\sum_{i=1}^{n} R_{zi}}{n}$ |
| $R_a$ | Roughness average $R_a$ is the arithmetic mean of the absolute values of the roughness profile ordinates | $R_a = \frac{1}{l_r} \int_0^{l_r} \lvert z(x)\rvert dx$ |

Yoshimi and Kishida (1981) defined the surface roughness with the reference value, which is the maximum height of the profile ($R_z$) along the 2.5-mm sample length (L) [74]. Uesugi and Kishida (1986) also used the maximum height of the profile ($R_z$) as the reference value, but the sample length is set as 2 mm or average particle size ($D_{50}$). Current research applies the normalized surface roughness ($R_n = R_{max}(L = D_{50})/D_{50}$ or $R_a/D_{50}$ or $R_q/D_{50}$) into the granular material and steel interface shear test [75–77].

Staheli et al. (2006) conducted interface shear tests using sand against various pipe materials, including wet cast concrete, vitrified clay, polycrete, and hobas, to determine the relationship between interface characteristics and construction behavior (see Table 3). The surface roughness (average roughness, $R_a$) of the pipe materials, as well as its corresponding friction coefficient ($\mu$, the ratio of shear stress to normal stress), were measured using a Taylor Hobson Form Talysurf Series 2 stylus profilometer. The friction coefficient increases as $R_a$ increases, as demonstrated by the test results.

**Table 3.** Effect of surface roughness on the friction coefficient with Ottawa sand at 40 kPa, 80 kPa and 120 kPa.

| Parameters | Hobas | Polycrete | Wet Cast Concrete | Vitrified Clay | Packhead Concrete |
|---|---|---|---|---|---|
| Average Ra (μm) | 6.5 | 16.9 | 18.7 | 24.8 | 55.1 |
| Friction coefficient (peak) (40 kPa) | 0.51 | 0.50 | 0.68 | 0.68 | 0.81 |
| Friction coefficient (residual) (40 kPa) | 0.43 | 0.42 | 0.49 | 0.49 | 0.54 |
| Friction coefficient (peak) (80 kPa) | 0.50 | 0.49 | 0.62 | 0.65 | 0.73 |
| Friction coefficient (residual) (80 kPa) | 0.44 | 0.43 | 0.44 | 0.48 | 0.53 |
| Friction coefficient (peak) (120 kPa) | 0.48 | 0.47 | 0.62 | 0.63 | 0.73 |
| Friction coefficient (residual) (120 kPa) | 0.42 | 0.43 | 0.47 | 0.45 | 0.52 |

Iscimen and Frost (2010) produced laboratory equipment to investigate the shear stresses at the pipe–soil interface for curved pipe surfaces [78]. It revealed that the shear strength of the soil–pipe interface was found to rise with increasing surface roughness up to a specific value, beyond which no effect on the shear strength was observed. Knappett and Craig (2012) concluded the previous research and demonstrated the relationship between various soil–material interfaces (Figure 7) [79]. These studies demonstrate that the increasing friction angle gradually approaches the soil internal friction angle until the surface roughness reaches a certain value, called critical roughness.

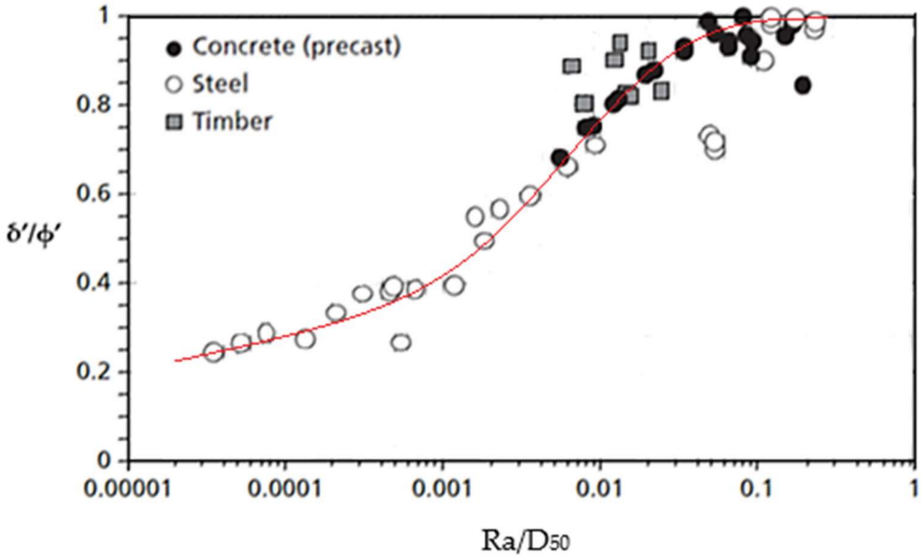


**Figure 7.** Interface friction angle for various construction materials.

### 3.1.2. Roughness Measurement

Before conducting interface shear tests, the microscopic surface roughness of a structural material must be determined to quantify its surface roughness with defined specific parameters that will affect soil–structure interface behavior. Roughness parameters are typically determined using a surface roughness tester and are quantified in terms of the average roughness (Ra, see Figure 8). Surface roughness testers consist of portable surface

roughness gauges and the three-dimensional microscope profilometer. Compared to 3D optical profilometers, portable surface roughness gauges (see Figure 9) provide a better cost–performance ratio, including the surface profile gauge (with a broad range and poor resolution) and the surface roughness gauge (low range and high resolution). As a result, portable surface roughness gauges are usually applied in industry and laboratories.

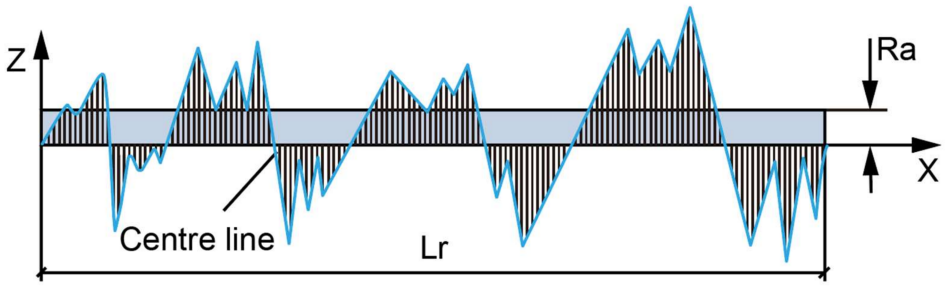


**Figure 8.** Schematic representation of average roughness, Ra.


(**a**)


(**b**)

**Figure 9.** Portable surface roughness gauge: (**a**) surface profile gauge (large range and low resolution); (**b**) surface roughness gauge (low range and high resolution).

However, the probe contact and manipulative interferometry technique cause the inaccuracy of the surface roughness result, which may not satisfy the high requirement on the resolution [80]. Thus, a 3D optical profilometer (a chromatic confocal apparatus) is applied for high-resolution results with the chromatic confocal imaging method and nonin-

trusive technology [81]. The 3D optical profilometer consists of confocal scanning and high chromatic aberration of the objective lens, which can measure various materials' roughness with the latest white light interferometry (WLI). The white light, transmitted through the profilometer's objective lens, is used to scan the material, generating a wavelength on the single monochromatic point in terms of the refractive index (see Figure 10). The image can then be obtained as image results via the formation of single monochromatic points, which is much more accurate than merely using mean surface roughness. Additionally, the reflectivity and absorption of the scanned sample have no effect on results, even if the material is transparent or specular.

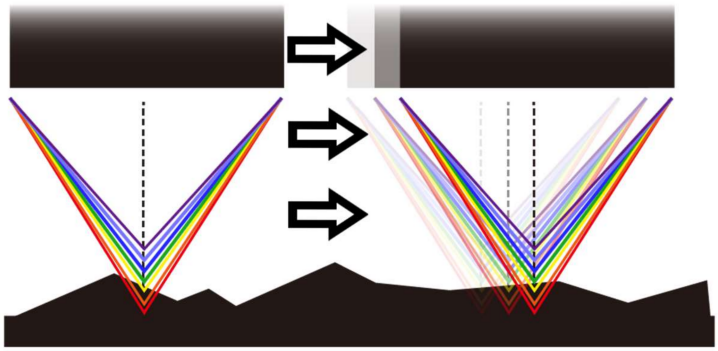

**Figure 10.** Various wavelengths on the single monochromatic point.

Sandpaper, a synthetic abrasive material, is manufactured with specified surface characteristics, which can be used to simulate a variety of materials, including vitrified clay pipe, precast concrete, polycrete concrete, Permalok steel casting pipe, and Hobas pipe [42]. However, previous research on sandpaper reveals that sandpapers of the same grit but manufactured by various companies have significantly variable surface roughness properties [81,82]. Thus, roughness characteristics should be determined using specialized instruments rather than simply defined by the company's marked grit level.

#### 3.1.3. Definition of Surface Roughness Form

Current research indicates that the critical surface roughness cannot limit the shear strength development under certain conditions caused by the additional passive resistance induced by interface clogging. Thus, surface roughness is classified as random or ribbed surface roughness form (clogging) or structured surface roughness form (non-clogging) [83].

The random or ribbed roughness form (Figure 11a,b) is widely applied for research into the behavior between soil–material friction, especially for precast concrete surface and flat metal surface. Researchers found a critical state for interface behavior, called critical roughness. The critical roughness is determined by the global behavior of the interface shear test and the reference values for surface roughness. According to research on the interface shear behavior between normal consolidated Kawasaki clay and steel, Tsubakihara and Kishida (1993) found that surface roughness increment led to the developed shearing resistance and interface sliding until the reference value reached the critical steel roughness. Once the reference value is over the critical steel roughness, shear failure exists in the clay instead of the soil–material interface. Therefore, for random or ribbed surface roughness form, the maximum interface strength equals the soil strength, called "$\delta = \varnothing$ condition", and the critical roughness is about half of the mean particle size ($D_{50}$) [83,84].

On the other hand, some researchers believe that the interface friction angle, caused by a highly rough structured surface (Figure 11c), is larger than soil internal friction angle in some specific loading conditions, which is called "$\delta > \varnothing$ condition" (interface friction angle > soil internal friction angle), especially for cast-in-situ concrete surface and patterned metal surface [85–87]. Mitchell and Villet (1987) found that the shear strength of the interface shear test was not only developed by interfacial friction between the sand particle and structure

surface as "δ = ∅ condition", but additional passive resistance generated [88]. Martinez and Frost (2017) defined two kinds of surface roughness forms, clogging-prone surface (random or ribbed roughness form) and non-clogging surface (structured roughness form), applied in sand–structure interface shear test [83]. Compared with structured roughness forms, random or ribbed roughness forms produce the interface clogging and restrict interface friction angle to soil internal friction angle.

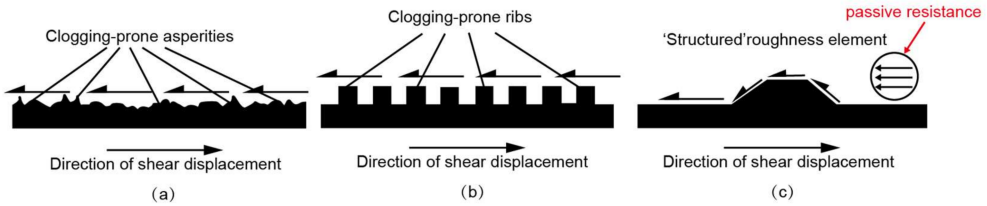


**Figure 11.** Load transfer mechanisms during shear against the surface of (**a**) random, (**b**) ribbed, and (**c**) structured roughness form.

The identification of clogging-prone and non-clogging surfaces helps researchers to determine the development of soil–material interface shear mechanism. Besides, it was also identified that the ratio of particle size to roughness height would affect the interface behavior, especially in terms of its induced shear forces. With the advanced technology recommended or applied in roughness measurement, surface form definition helps to quantify the surface roughness for more accurate and reliable use in soil–structure interactions.

### *3.2. Influence of Other Factors on Interface Behavior*

#### 3.2.1. Particle Angularity

The shapes of the particles have a significant impact on the shear behavior of granular materials [89–91]. Particle shapes are described by roughness, roundness, texture, and sphericity [92]. Uesugi and Kishida (1986) found that particle angularity greatly affected the pipe–soil interface shear strength, as angular particles interlock more strongly than rounded particles. Consequently, it is critical to describe the particle angularity during the analysis of frictional forces. Particles can be characterized according to their angularity as rounded, subrounded, angular, or subangular: (1) angular particles have relatively rough flat surfaces and sharp edges; (2) subangular particles have rounded edges; (3) rounded particles have smooth curved sides that lack edges; and (4) subrounded particles have well-rounded corners and edges, but almost flat sides [93]. Figure 12 illustrates the various particle shape classifications.

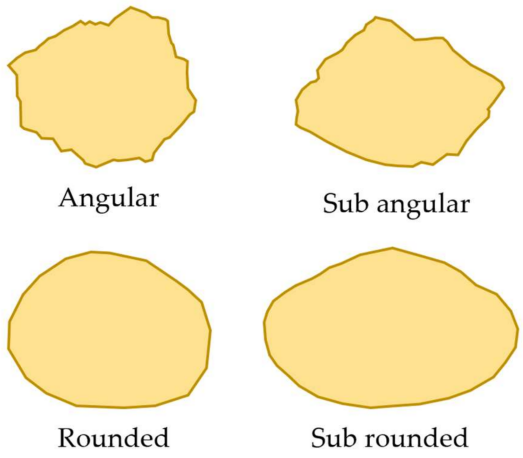


**Figure 12.** Classification of particle shape as angular, subangular, rounded and subrounded.

According to previous studies, increasing the angularity and decreasing the roundness can result in larger maximum ($e_{max}$) and minimum ($e_{min}$) void ratios, respectively [92,94]. Cho et al. (2007) described particle shape and surface roughness analysis as examining the relationship between particle shape, stiffness, packing density, and sand strength, whilst taking into account the particle's roundness, sphericity, and smoothness. When exposed to increasing particle irregularity, it was revealed that $e_{max}$ and $e_{min}$ increased, while the critical state friction angle and compressibility decreased.

Angular quarry materials demonstrated greater shear strength when compared to a combination of subrounded to subangular gravel and sand in triaxial tests [95]. Edil et al. (2006) conducted a series of research on interface shear tests with various particle angularities and particle sizes. They found that the increment in particle angularity leads to a more significant particle interlocking and higher peak shear strength. Additionally, the angular granular material requires a larger shearing displacement to reach peak strength. Li et al. (2013) studied the peak and constant-volume friction angles in a clay gravel combination by adjusting the gravel content. It was found that increasing the asymmetry and roughness of the gravel particles resulted in an increase in constant volume friction angle and a reduction in peak friction angle.

Peerun et al., (2019) investigated the shear behaviors of granular tunneling spoil by comparing rounded sand-based sandstone particles with angular shale particles with lower carbonaceous mineral contents (see Figure 13). Table 4 summarizes the data on vertical stress acting on the pipe. Due to the strong rounded particles of sandstone, higher dilation occurred, and friction angles of 40.5° and 28.6° were measured for pipe-jacking Drives C and D, respectively, in their study [30]. The two pipe-jacking drives had apparent cohesion values of 11.9 kN/m$^2$ and 17.3 kN/m$^2$, respectively. The vertical tension acting on the pipes was computed using the Pellet-Beaucour and Kastner (2002) jacking force model (Equation (8)). Pipe-jacking Drives C and D [30,96], in their study, encountered low positive vertical stresses, $\sigma_{EV}$ of 15.3 kN/m$^2$ and 12.1 kN/m$^2$, respectively, indicating that less arching occurred due to the low $\sigma_{EV}$ values.

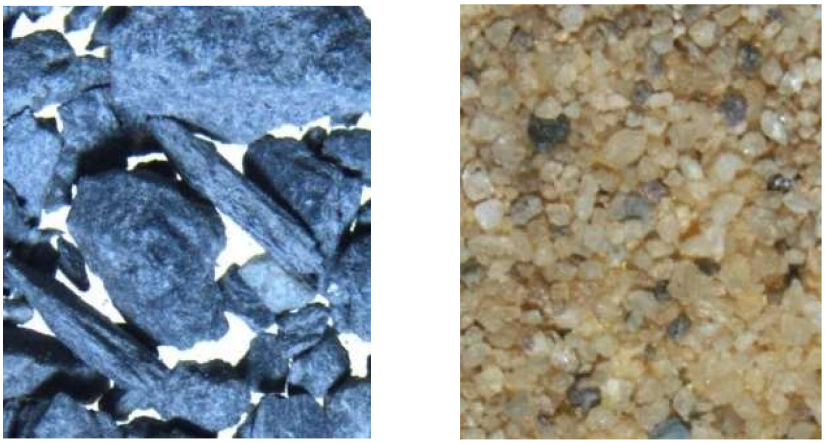

(**a**) (**b**)

**Figure 13.** The difference in particle angularity between (**a**) shale (angular) and (**b**) sand (subrounded).

Note: Pellet-Beaucour and Kastner (2002) use Equation (8) to describe the vertical soil stress experience at the pipe or tunnel crown due to the arching effect.

$$\sigma_{EV} = \frac{b\left(\gamma - \frac{2C}{b}\right)}{2K \tan\Phi}\left(1 - e^{-2K\frac{h}{b}\tan\Phi}\right) \quad (8)$$

where:

C—soil cohesion;

Φ—soil internal friction angle;
γ—soil unit weight;
K—lateral earth pressure coefficient;
h—soil cover from the ground level to the pipe crown;
b—influencing soil width above the pipe.

**Table 4.** Assessment of vertical stresses acting on pipe crown.

| Parameters | Symbol | Unit | Drive C | Drive D | Drive E | Drive F |
|---|---|---|---|---|---|---|
| Geology | - | - | Sandstone | | Shale | |
| Soil friction angle | ϕ | degree | 40.5 | 28.6 | 37.3 | 37.3 |
| Soil cohesion | C | kPa | 11.9 | 17.3 | 0.0 | 0.0 |
| Arching | - | - | Low to moderately favorable | | Least to not favorable | |
| Calculated vertical stress on pipe crown | σ | $kN/m^2$ | 15.3 | 12.1 | 34.8 | 42.9 |
| Average volume of lubricant used | - | L/m | 250 | 250 | 500 | 375 |
| Average jacking speed | - | mm/min | 29.2 | 22.4 | 10.4 | 18.9 |
| Measured jacking force | JF | kN/m | 10.1 | 18.9 | 29.0 | 28.5 |

On the other hand, angular particles of shale formed a high void ratio and were more vulnerable to compression [30]. As such, particle breakages were postulated, which may have contributed to the decrease in peak shear stresses and apparent cohesion [30]. According to Equation (8), soil cohesion and internal friction angle have significant effects on the vertical soil stress acting on the pipe, with vertical soil stresses, $\sigma_{EV}$ = 34.8 $kN/m^2$ for Drive E (shale) and $\sigma_{EV}$ = 42.9 $kN/m^2$ for Drive F (shale). In comparison to sandstone (pipe-jacking Drives C and D), pipe-jacking Drives E and F [30,96] in shale sustained much greater vertical stresses, implying a lesser arching state, and thus greater friction developed between pipe surface and shale. This would indicate that the jacked pipes came into contact with the surrounding geology, resulting in increased frictional resistance. This is supported by the substantially higher observed jacking forces (JF) for shale drives (JF = 29.0 kN/m and 28.5 kN/m) compared to sandstone drives (JF = 10.1 kN/m and 18.9 kN/m). Ong and Choo (2018) found similar observations as well [97]. These consistent observations indicate that the angularity of particles does affect the development of the load transfer mechanism and the mobilization of loads between soil–pipe (structure) surfaces.

#### 3.2.2. Mean Particle Size

Subba Rao et al. (1998) found that particle size greatly affects soil internal friction angle, and simply classifying the structure surface with roughness parameters may not be reasonable. Thus, the assessment of interface shear test results requires a newly defined parameter, which is the normalized roughness, defined as the ratio of the average roughness and the mean particle size ($D_{50}$). Vangla and Gali (2016) demonstrated that the fitness between the mean particle size of granular material and material roughness contributes to the particle interlocking, and thus fully develops the interface shear strength [98]. Additionally, Punetha et al. (2017) found that the effect of mean particle size depends on the material texture [99]. The mean particle size produced a slight effect on soil–geomembrane interface behavior, but a significant effect on the soil–geotextile interface behavior. With mean particle size increment, the contact stress per particle is reduced for the soil–geotextile interface behavior. Sand–steel interface shear test reveals that the increment in mean particle size has a slight effect on friction development, and the friction angle from the interface shear test is much lower than soil internal friction angle [100]. These outcomes demonstrate that

the mean particle size influences the interface shear mechanism corresponding to surface roughness and material texture.

#### 3.2.3. Surface Hardness

Surface hardness is one of the essential factors dictating mechanical interface behavior in tribology [101]. Frost et al. (2002) demonstrated the effect of the material hardness on the soil–material interface behavior. According to the plot of peak secant friction coefficient (tan $\delta$) versus normal stress (see Figure 14), the interface shear resistance dwindles at the initial state and rebounds after achieving critical normal stress. At the initial state, the contact area between each granular particle and material surface is increased with lower normal stress. Thus, the effective shear stress of the particle is decreased until the contact area reaches the specific value. Once the normal stress reaches the limit state, additional increments of normal stress cause particle movement and particle plowing, leading to shear stress increasing [51]. Thus, the design of the substructure with low overburden pressure (or normal stress) requires a further investigation on surface hardness, which affects plowing behavior.

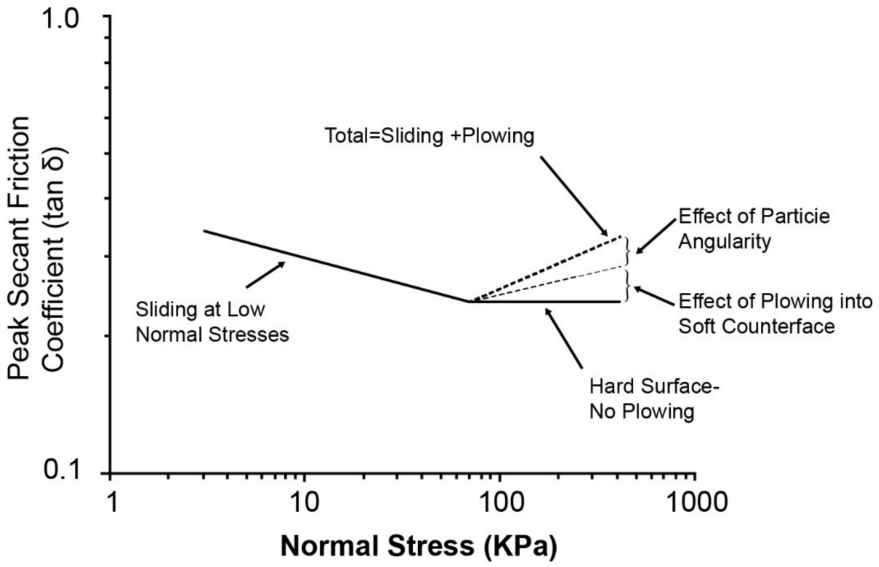


**Figure 14.** Normal stress versus friction coefficient for soil–continuum material interfaces.

#### 3.2.4. Particle Breakage

For the large-displacement shear test, the plowing and sliding in the interface shear test leads to significant particle breakage, which converts the soil mechanical property, changes the frictional behavior, and contributes to shear zone development [49]. A soil sample with a high void ratio and angular particles is more likely to break and experience a decrease in the internal friction angle of the specimen [29,30,102]. Peerun (2016) researched metagraywacke and shale specimens using direct shear tests. The specimens have low dry densities and high void ratios due to their rough-surfaced angular particles. The higher void ratios and poorer mineralogy of the particles resulted in anticipated particle breakages, which drastically decreased the beneficial particle interlocking phenomenon. Thus, using the flaky metagraywacke and shale particles as examples, low interlocking activity has resulted in reduced apparent cohesion, and thus less opportunity for strength development. Particle breakage remains an extreme challenge to measure, especially when tests are performed in the small shear box; thus, the use of discrete element modeling (DEM) may help solve this problem. DEM shall be discussed later in the paper.

3.2.5. Confinement Condition

According to various research requirements, interface shear apparatus is manufactured based on conventional shear techniques, which include direct shear apparatus, simple shear apparatus, and ring shear apparatus. Thus, confinement conditions vary in interface shear tests, owing to the different limitations of the shear apparatus. Other than the restrictions of the apparatus, the shear mechanism is also affected by the normal stress applied to the soil specimen. At higher normal stresses, a soil sample will experience increased compression and particle interlocking, resulting in a greater specimen shear strength [102,103]. Thus, it is critical to match the interface shear apparatus and normal stress range to the actual site conditions.

## 4. Potential Application of Particle Image Velocimetry (PIV) Technology for Research on Interface Friction

### *4.1. Background*

Particle image velocimetry (PIV) technology was developed by Adrian (1991) and based on laser speckle velocimetry, which measures the velocity of solid or fluid via an illumination system and two consecutive particle images [104,105]. White and Take (2002) introduced the principle of PIV technology (see Figure 15) and provided a Matlab module (GeoPIV) to analyze geotechnical displacement [106].

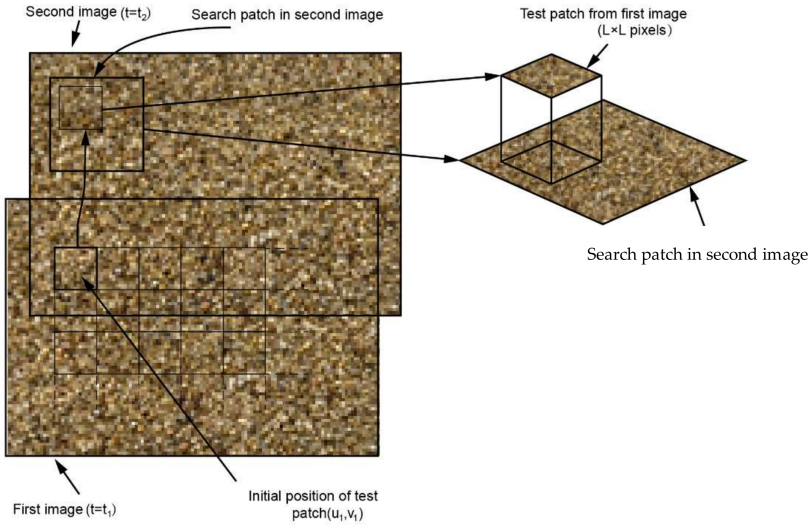


**Figure 15.** The principles of PIV technology.

Numerous researchers have investigated particle behavior along with shear bands. Laboratory studies and numerical modeling are often used to better understand particle behavior during shearing [29,30,107–109]. Peerun et al., (2019) revealed that such investigations have several limitations, including the following: (1) numerical simulations reveal the nonuniformity of stress generated during direct shear testing [110,111]; (2) restricted views of shear zones caused by equipment fittings [112]; (3) sporadic observations of shear band formation and particle activity [113,114]; and (4) studies on granular material are constrained to plane-strain assumptions [115]. These known constraints impede the physical testing requirements for experimental validation of predicted particle behaviors and for providing continuous and unobstructed views of granular materials during shearing when advanced image processing techniques are used to develop an in-depth understanding of surface roughness.

Peerun et al., (2019) addressed the difficulties associated with obtaining clear evidence of test specimens during shearing in order to examine particle movements along the shear zone. This was achieved by continually capturing high-resolution photographs during direct shear testing on actual granular materials using a fully transparent shear box. Although

particle image velocimetry (PIV) is not a technological evolution, the supplemental use of PIV in validating a conventional shear box test and then utilizing interpreted parameters and techniques developed for proper interpretation of actual soil–structure interactions, i.e., pipe jacking operations [29,96,97,116,117], is novel and significant in terms of developing basic knowledge in the field of study of the development of interface friction.

### *4.2. Introduction*

The success of the above-mentioned tests and observations on the reliable use of PIV technology have led the authors to explore the possibility of further modifying the interface direct shear test to examine, quantify, and verify the specific relationship between soil–structure interaction and structural surface roughness. In order to investigate the sand–material interface shear mechanism under high normal stress, interface direct shear apparatus is conducted based on small-scale direct shear apparatus. In addition, this conceptual idea can be in the form of replacing the bottom shear box with the solid block. Furthermore, PIV technology is applied to obtain particle movement by replacing the opaque metal shear box with a custom-made, transparent Perspex (resin) shear box. The random or ribbed surface roughness of any structural surfaces can then be assessed using a portable surface roughness gauge, which includes a surface profile gauge (with a wide range and low resolution) or a surface roughness gauge (with a low range and high resolution).

The interface direct shear test consists of a series of parametric studies using sand and sandpaper interface for calibration (Figure 16a), and then performing a validation study using the same sand but with the sandpaper being replaced by a structural material interface (Figure 16b), each of which utilizes a specific bottom shear box. Parametric research was conducted using the results of interface direct shear tests to determine the relationship between the defined roughness parameters (sandpaper grit is readily available or can be easily confirmed with a profilometer) and the soil–sandpaper interface shear mechanism. The interface behavior between soil and structural material is then validated with the four-stage model, corresponding to parametric research.

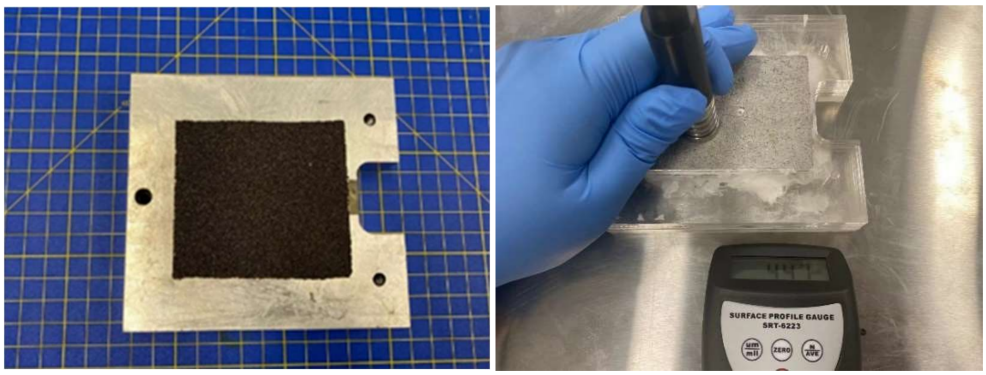


(**a**) (**b**)

**Figure 16.** (**a**) Sandpaper glued on the bottom shear box; (**b**) material block cast by concrete.

### *4.3. Tested Material*

The granular material (coarse sand) collected from the Logan River system of Queensland is categorized as poorly graded sand (UCSC) and subrounded particles (ASTM D2488, see Figure 17), which is used for the interface direct shear test with Australia standard. Based on soil compaction and density test standard (AS1289.5.5.1), the maximum and minimum void ratios are 0.62 and 0.46, respectively. The sieve test reveals that the mean particle size of granular material is 0.833 mm. The coefficient of uniformity (Cu) and coefficient of gradation (Cc) are 1.44 and 1.01, respectively. Previous research on interface shear tests shows that the relationship between particle size and surface roughness is roughly estimated [46,78]. Thus, the critical surface roughness determined in this research may range from 13μm to 415μm. Additionally, fundamental research requires a portable surface

roughness gauge with a large measurement range and high resolution. Thus, surface roughness gauge (SRG) (see Figure 9b and Table 5) with a low range and high resolution is applied for determining smooth surface roughness (sandpaper with grit 180 and grit 360) in this research. Meanwhile, due to the limited measurement range of surface roughness gauge, the surface profile gauge (SPG) (see Figure 9a and Table 6) with a wider range but poorer resolution is applied for measuring the rough surface (concrete block, sandpaper with grit 40 and grit 80). The sandpaper and the structural material roughness parameters are provided in Table 7.


**Figure 17.** Particle shape extraction of tested material using a microscope.

**Table 5.** General specifications of the surface roughness gauge SRG-4600.

| | |
|---|---|
| Measures grooves and recessions: | wider than 0.16 in (4 mm) |
| Roughness parameters: | Ra, Rz, Rq (Rms), Rt, Rs, Rsm, Rmax, Rpc, Rmr. |
| Roughness standards: | ISO/DIN/JIS/ANSI |
| Display resolutions: | 0.01µm/±20 µm 0.02 µm/±40 µm 0.04 µm/±80 µm |
| Measuring accuracy: | ≤±10% |
| Repeatability: | Less than or equal to 6% |
| Measuring range: | Ra, Rq: 0.01–40 µm Rz, Rt, Rm: 0.02–160 µm |
| Maximum drive range: | 0.7 inch (17.5 mm) |
| Cut-off length: | 0.009/0.03/0.09 inch (0.25/0.8/2.5 mm) |
| Tracing speeds: | speed 1 mm/s (sampling length 2.5 mm)<br>speed 0.5 mm/s (sampling length 0.8 mm)<br>speed 0.135 mm/s (sampling length 0.25 mm) |
| Sensor: | Inductance type |
| Sensor-stylus: | Diamond, radius 5 µm |
| Pick up Force: | <4 mN |
| Filter: | RC, PC-RC, GAUSSIAN, and D-P |
| Data output: | USB |
| Operating temperature: | 41–104 °F (5–40 °C) |
| Weight: | 0.97 lb (440 g) |
| Dimensions: | (119 × 47 × 65 mm) |
| Power: | Li-Ion rechargeable battery |

**Table 6.** General specifications of the surface profile gauge SRT-6223.

| | |
|---|---|
| Display: | Four digits, LCD |
| Range: | 0 µm to 800 µm (0 mils to 30 mils) |
| Accuracy: | ±5% or ±5 µm, (whichever is the greater) |
| Resolution: | 1 µm (0.1 mils) |
| Measurement speed: | >30 readings per minute |
| Weight: | 280 g |
| Dimensions: | 162 × 65 × 28 mm (6.4 × 2.6 × 1.1 inch) |
| Operating temperature: | 0 °C to 50 °C, <80%RH |
| Batteries: | 4 × 1.5v (AAA) battery |

**Table 7.** Material roughness parameters.

| | Ra | Rq | Rz | Rmax | $D_{50}$ (CS) | Rn |
|---|---|---|---|---|---|---|
| Structural material | N/A | N/A | 422 | N/A | 833 | 0.507 |
| Grit 40 Sandpaper | N/A | N/A | 722 | N/A | 833 | 0.867 |
| Grit 80 Sandpaper | N/A | N/A | 460 | N/A | 833 | 0.552 |
| Grit 160 Sandpaper | 20.07 | 26.63 | 81.66 | 123.3 | 833 | 0.148 |
| Grit 320 Sandpaper | 10.96 | 13.37 | 29.39 | 58.0 | 833 | 0.070 |

Note: "N/A" means "Not within measuring range".

### *4.4. Equipment Setup*

#### 4.4.1. Transparent Shear Box

A 60-mm square shape shear box (see Figure 18a) produced by Gilson Company consists of a top and bottom shear box, connected with two location screws. Four lifting screws of the shear box adjust the gap between the top and bottom shear box. As the conventional shear box is made of steel, the behavior of particles along the predetermined shear band thickness is, thus, invisible. To detect how geomaterial particles shear and flow around the interface, a transparent shear box (see Figure 18b) made of high-strength plastic resin is manufactured for this conceptual study. Compared with the initial shear box, three location screws are applied on the transparent shear box to analyze the interface behavior. The modification includes extending the maximum shear displacement from 8 mm to 15 mm, which ensures that effective shearing would encompass the development of residual strength [70].

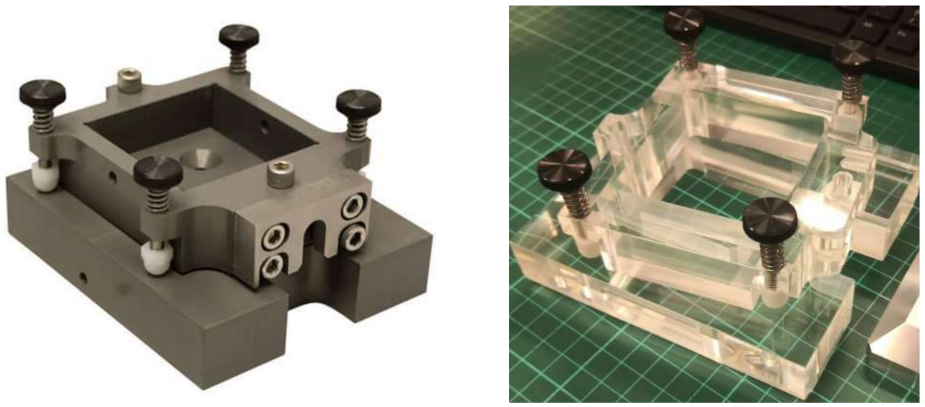

(**a**) (**b**)

**Figure 18.** (**a**) A 60-mm (2.36 in) shear box (HMA-734MS) and (**b**) custom-made 60-mm (2.36 in) transparent shear box by the authors for preliminary interface shear study.

4.4.2. Camera and Illumination System

A Canon EOS 90D Digital Single Lens Reflex (DSLR) camera is installed on the aluminum clamp with a bottom screw and applied to capture the interface behavior between the top and bottom shear box, which provides high-resolution photos with a 32.5-megapixel APS-C size sensor. However, the camera installation is limited by several factors, such as the shear box displacement, the testing space, the loading frame capacity, the dimensions, and focal length of the camera. After several trial tests, the window dimension of the modified loading frame and water chamber is produced at 110 mm × 40 mm (Figure 19a) and 140 mm × 40 mm (Figure 19b), respectively. Meanwhile, the displacement between the modified loading frame and the camera body is 260 mm.

(**a**) (**b**)

**Figure 19.** Custom-made (**a**) modified loading frame and (**b**) modified water chamber by the authors for preliminary interface shear study.

The film sensitivity of Canon EOS 90D leads to a large expandable ISO speed, which represents a high "light gathering" ability. However, the film's sensitivity is not significant enough to capture high-resolution images in darkness. Meanwhile, the original laboratory environment light causes the shadow to form over part of the critical image. Thus, a new illumination system is set up using a 152-mm ring light and an Elgato multi-mount kit (see Figure 20). Furthermore, to avoid the disturbances caused by the manual operation on the camera, Canon support software (EOS Utility) is used to remotely control the automatic and sequential capture of the images.

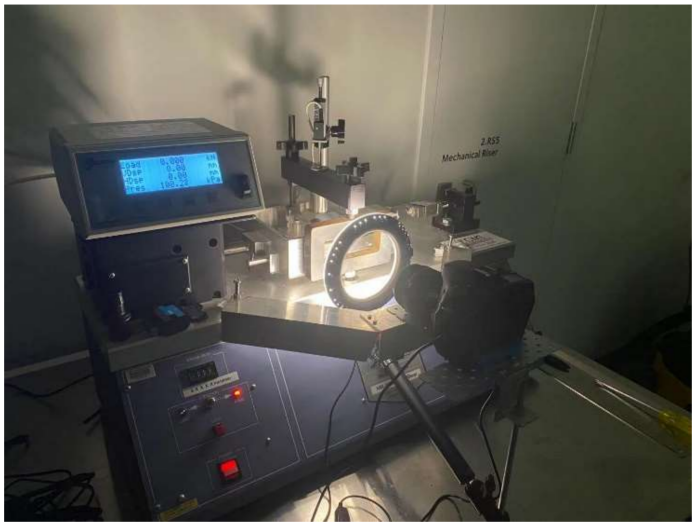

**Figure 20.** Custom-installed illumination system by the authors for preliminary interface shear study.

4.4.3. Modified Loading Frame

Previous research found that the horizontal force of the direct shear test causes the nonuniform stress on the inner side of the shear box and interrupts the accuracy of the measurements [29,52,58,70]. Preparatory experiments demonstrated that the conventional direct shear test with a free top plate would result in an uneven loading plate when the large normal stress is applied on the soil sample (see Figure 21a). Jewell (1989) found that a free loading plate leads to a higher peak shear strength than a fixed loading plate due to the free particle movement of the interlocking stage (see Figure 22) [118]. Thus, a fixed connection (see Figure 21b), instead of a ball bearing, is customized and manufactured between the loading frame and shear box, providing the symmetric normal stress and limiting the top plate rotation. A similar improvement of the loading frame has been adopted in the study by Peerun et al. (2019).

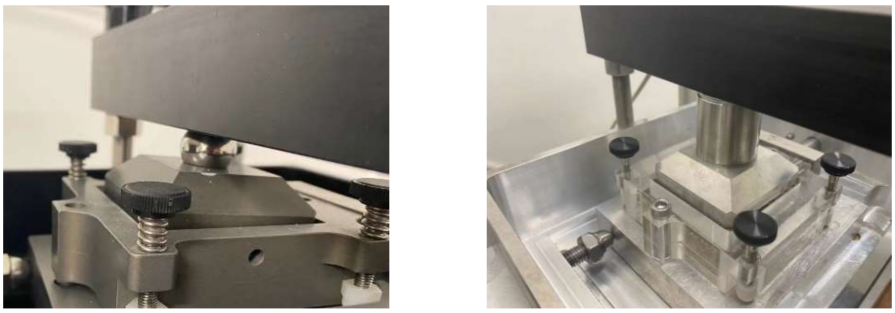

(**a**) (**b**)

**Figure 21.** (**a**) Conventional free loading plate and (**b**) custom-made fixed loading plate by the authors for preliminary interface shear study.

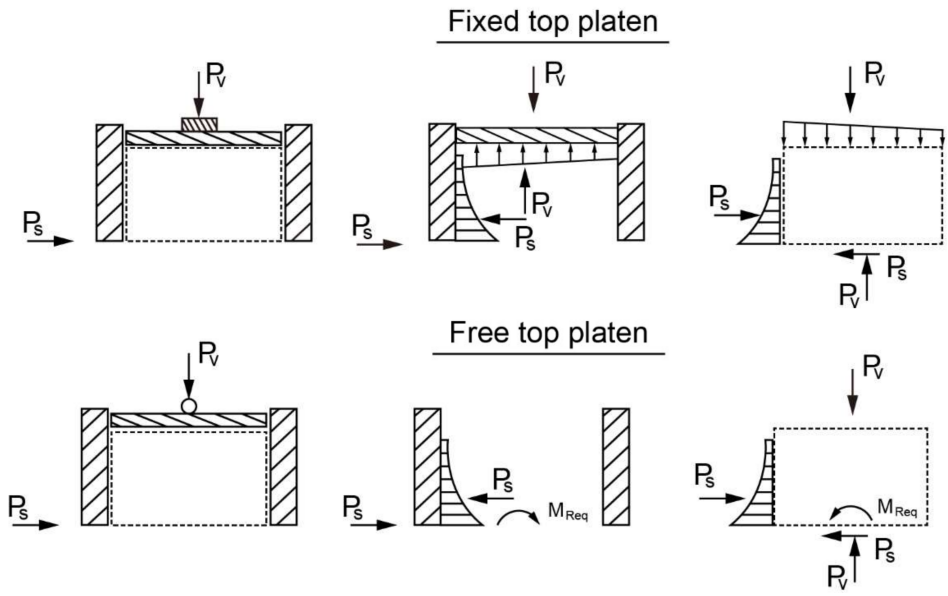


**Figure 22.** Stress distribution for free loading plate and fixed loading plate.

4.4.4. Procedure of Interface Direct Shear Test

The soil sample is prepared with the dry pluviation method or compaction method for different relative densities. The shearing rate, the maximum horizontal displacement, and the shear box gap are preliminarily set as the aforementioned direct shear test. However, since the residual shear strength cannot be determined with the limited horizontal displacement, the maximum horizontal displacement is expanded in the interface shear test. The procedures of the interface shear test are shown below:

1. For abrasive material, clean the modified bottom shear box with acetone in the fume cupboard (Figure 23), and stick the sandpaper on the modified bottom shear box with proper location.
2. For reinforcing material, put the sample block into the modified bottom shear box.
3. Adjust the lifting screw and clamping screws to suit the 0.6 mm steel plate between the top and bottom shear box, and remove the steel plates.
4. Fix the base plate and the perforated grid plate, and the shearing force is perpendicular to a serration orientation.
5. Fill the soil sample with 14.5-mm thickness with dry pluviation method or compaction method, and slightly put a porous stone on the sample.
6. Clean the bottom shear box and water chamber.
7. Measure the total weight of the shear box, and then place the assembly into the water chamber, slotting the end onto the pushrod.
8. Fix the horizontal and vertical LVDTs on the specific location and return records to zero.
9. Apply normal stress and wait until consolidation is completed (cohesionless soil is consolidated instantaneously).
10. Remove clamping screws.
11. Shear the soil specimen with the constant rate ($R_d$).


(**a**) (**b**)

**Figure 23.** (**a**) Acetone for cleaning the metal block and (**b**) premium fiberglass fume cupboard used during the author's preliminary interface shear study.

### *4.5. Application of PIV in Interface Shear Tests*

Test results reveal that the interface shear strength is enhanced with the increment in surface roughness and gradually approaches soil shear strength (see Figure 24 and Table 8). In these cases, the coarse sand particles are observed to be much bigger and coarser than all the sandpapers used; hence, the results are intuitively correct. Therefore, it is evident that the increment in surface roughness leads to greater improvement on peak friction angle than residual friction angle (see Table 8).

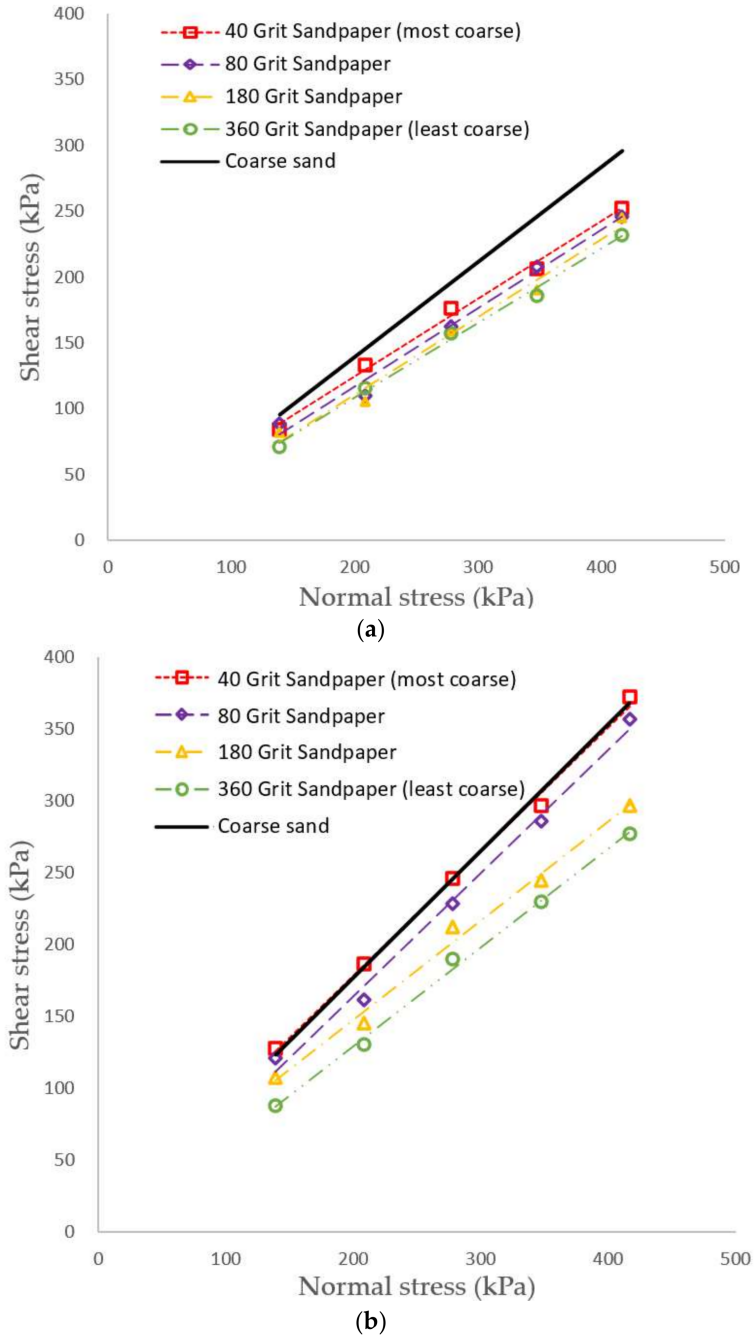


**Figure 24.** Measured soil internal friction angles and soil–material interface friction angles at (**a**) peak state and (**b**) residual state in the authors' preliminary interface shear study.

**Table 8.** Results of the soil internal friction angles (sand only) and soil–material interface friction angles (sand–sandpaper).

| Soil Type | Material Type | $D_{50}$ or $R_{max}$ (Micron) | Peak Friction Angle (deg) | Residual Friction Angle (deg) |
|---|---|---|---|---|
| Coarse sand | Coarse sand only | 833 ($D_{50}$) | 41.3 (sand only) | 35.8 (sand only) |
| Coarse sand | Grit 40 sandpaper | 722 ($R_{max}$) | 40.8 (sand–sandpaper) | 30.5 (sand–sandpaper) |
| Coarse sand | Grit 80 sandpaper | 460 ($R_{max}$) | 40.6 (sand–sandpaper) | 30.7 (sand–sandpaper) |
| Coarse sand | Grit 180 sandpaper | 81.66 ($R_{max}$) | 34.6 (sand–sandpaper) | 30.5 (sand–sandpaper) |
| Coarse sand | Grit 360 sandpaper | 29.39 ($R_{max}$) | 34.5 (sand–sandpaper) | 29.5 (sand–sandpaper) |

Particle image velocimetry (PIV) technology is applied to capture the particle microstructure and study the shear mechanism on different soil–reinforcement interactions. The interface shear responses (see Figure 25a), such as contraction and dilation of the soil sample, are validated by analyzing the particle interlocking, rotation, and possibly breakage behaviors. The four-stage model explains particle movement (see Figure 25b) corresponding to the stress–strain relationship of the soil sample. During stage 1 (end zone deformation), particles rearrange and move to the left, with slight vertical movement. During stage 2 (particle interlocking), the vector plot shows that localized particle interlocking at the left end of the shear box leads to 0.19 mm dilation through the soil sample. The particle interlocking prevents particle displacement and further develops the shear resistance to reach the peak state. During stage 3 (shear zone formation), small particles filled into the soil void and rotated large particles readjust the soil sample structure, which reduces the shear resistance and increases volumetric strain. Finally, during stage 4 (steady shear), the shear strain plot reveals that the soil sample generates a stable shear zone along the predetermined failure plane, causing nearly constant shear stress.

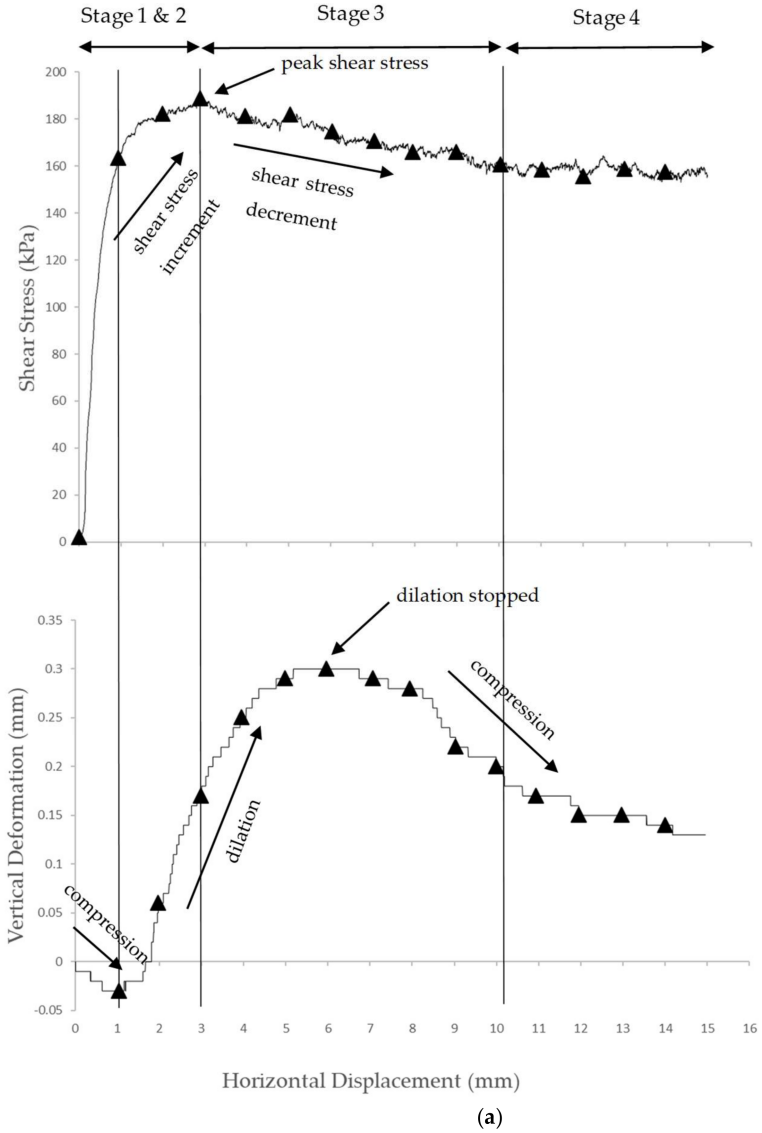


(**a**)

**Figure 25.** *Cont.*

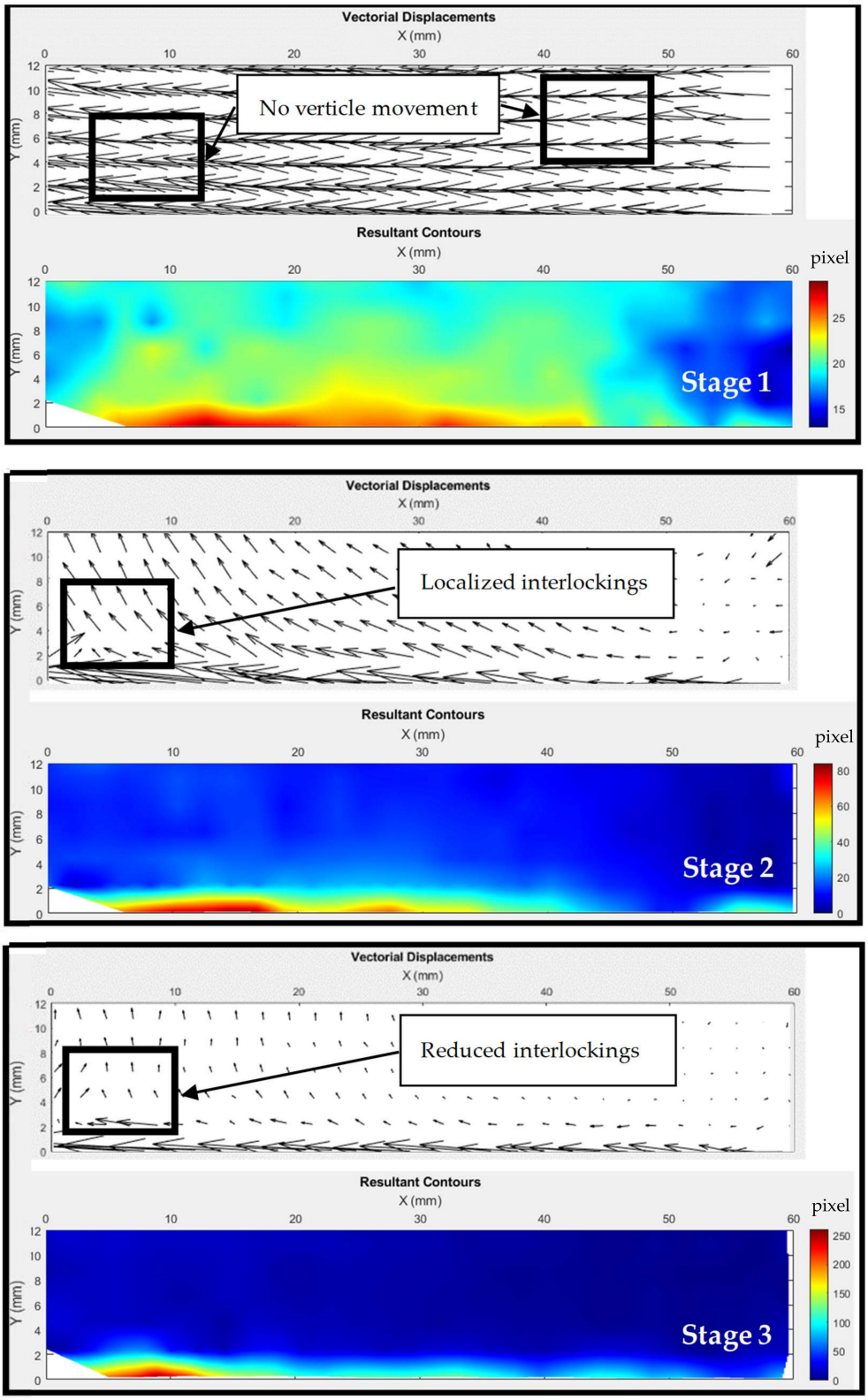


**Figure 25.** *Cont.*

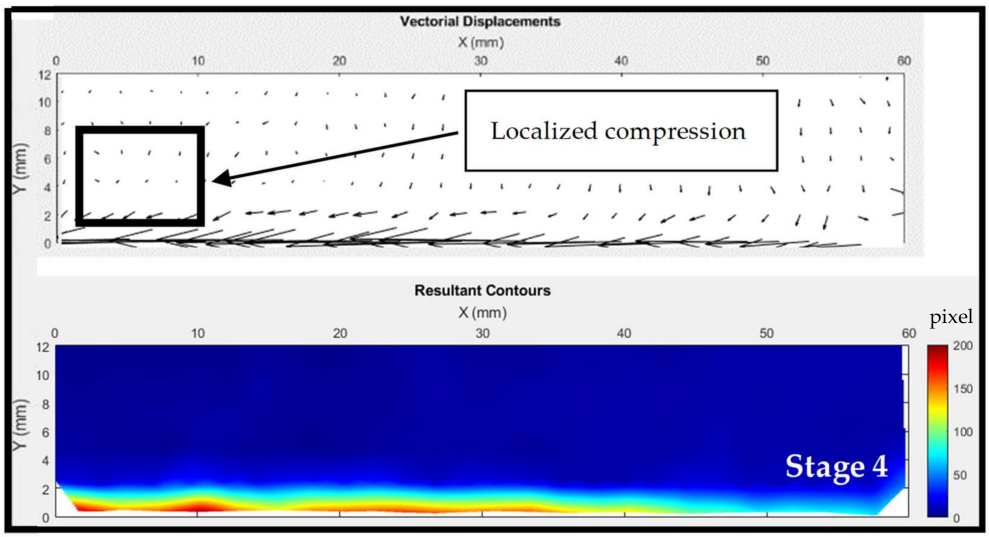


(**b**)

**Figure 25.** (**a**) Interface shear test results and (**b**) corresponding GeoPIV-RG results for Grit 360 sandpaper at 278 kPa normal stress in the authors' preliminary interface shear study (one pixel is equal to 15.79 micron).

The interface shear responses (see Figure 25a) validate the previous research on the effects of surface roughness. To further explore the coupling effect of particle size and surface hardness, granular material with different particle size distribution and recent advances can be applied in future research for greater accuracy. PIV analysis (see Figure 25b) reveals that the particle behavior of the interface shear test is similar to that of the direct shear test. Shear zone development in interface shear tests contributes to the understanding of soil–material interface behavior.

## 5. Recent Advances in Shear Strength Characterization

Interface shear test is a fundamental testing method to investigate soil–structure interactions. The use of the reliable PIV technique in interface shear tests is well-established and serves as the main verification strategy in this review paper to improve confidence levels and the justification of particle movements and interlocking behavior that help explain friction development in the shear box. Recent advances in shear strength characterization are not limited within the understanding of PIV application only, but also in other up-and-coming methods, such as artificial neural network (ANN), DEM, 3D printing, and Bayesian machine-learning method. These advanced methods also have great potential for applications for shear strength characterization and, thus, shall be reviewed in this paper as well.

### *5.1. Neural Network*

The aforementioned research found that the mutual coupling effect of surface roughness and other factors on the interface shear mechanism requires a greater understanding instead of the effect caused by the single factor. Meanwhile, the influence factors on interface shear mechanism are determined from laboratory tests and geotechnical investigations, and then applied for preliminary design. Even the standards normally provide a conservative design to ensure construction safety. Geotechnical engineers still require a method to accurately predict substructure performance to save construction costs [119].

Artificial neural network (ANN), a computational method based on empirical data, is widely applied as an alternative and as stochastic algorithms in the engineering field, such as material modeling, damage assessment, structural analysis and design, seismic liquefaction assessment, and ocean monitoring [120]. It is thought that machine learning methods such as ANN can be developed to consider the various influencing factors so

that the model can be used to predict the often elusive interface shear forces during soil–structure interactions as a result of understanding interface shear behavior. ANN imitates the nervous system (Figure 26a) to acquire knowledge and make conclusions that automatically deal with complex and challenging work [121]. ANN produces a nonlinear relationship by partially or fully connecting input variables (influence factors) and output variables (construction performance, e.g., interface shear) with one or more hidden layers (Figure 26b), corresponding mathematical functions, and Monte Carlo simulation [122].

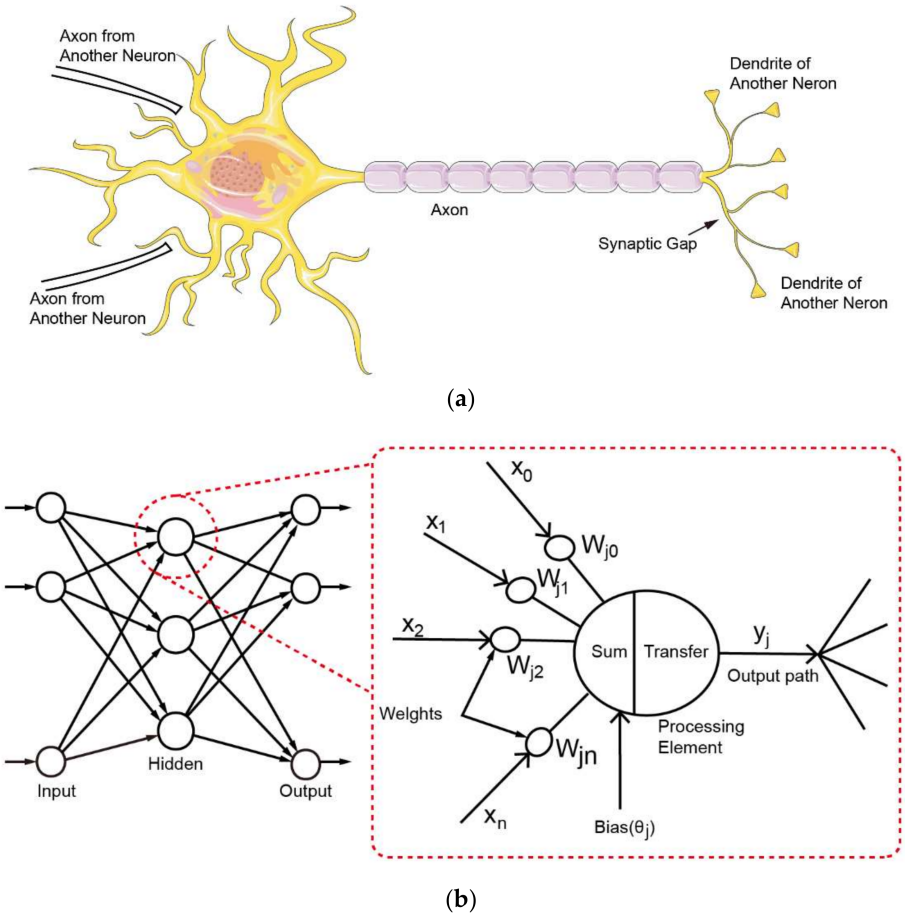


**Figure 26.** (**a**) Typical structure of biological neuron; (**b**) typical structure and operation of ANN.

### *5.2. DEM and 3D Printing*

Due to the challenges in maintaining identical test consistencies while performing parametric analyses involving interface shear tests, the discrete element method (DEM) can be used to perform virtual parametric studies based on the influences of different surface hardness on tested construction materials so as to develop a better understanding of complex interface shear mechanisms, such as the cone-penetration testing and pipe-jacking [107,123]. Additionally, instead of the spherical model often used in DEM, a micro-CT-scanned 3D model of the actual particle shapes can improve the simulation quality. Furthermore, calibration of interface shear tests using 3D printing of synthetic particles on different material surfaces can nowadays be readily executed in order to validate the DEM results [31,106,108,109]. For example, Figure 27 shows (a) a sandstone particle that was scanned using micro-CT to obtain its (b) particle shape in a triangular mesh format, and the latter was used to (c) 3D print a synthetic sandstone particle using polyamide material.

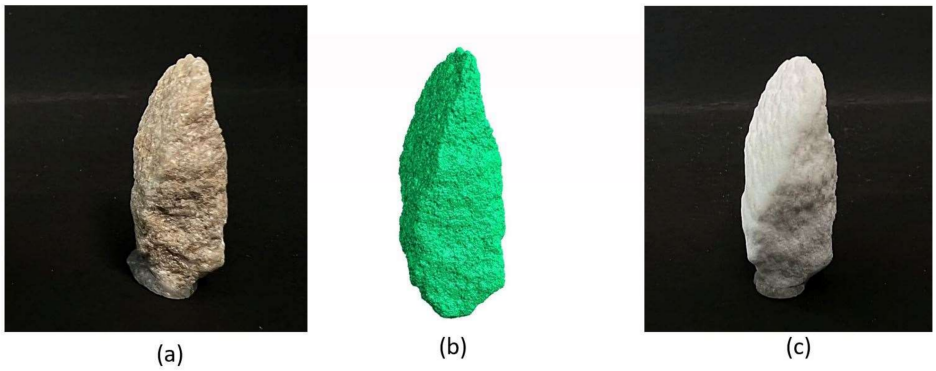


**Figure 27.** Particle shape extraction using micro-CT and printed synthetic particles for calibration of DEM: (**a**) a sandstone particle, (**b**) similar particle in a triangular mesh format, and (**c**) 3D-printed synthetic sandstone particle using polyamide printing material.

DEM is a numerical technique that was developed specifically for the purpose of resolving issues involving discontinuous materials. A jointed rock consists of discrete rock blocks and joint surfaces that enable the rock blocks to move, rotate, and deform while the joint surfaces may be squeezed, detached, or slid. The rock mass is considered a discontinuous discrete media, and its interior may be separated by large displacement, rotation, slide, and breakage, allowing it to more accurately simulate the nonlinear large deformation features of jointed rock. The discrete element method provides a series of physical parameters, such as speed, acceleration, angular velocity, line displacement, and rotation angle.

However, the majority of DEM models rely on limited experimental results for calibration and validation at the granular scale [124,125]. Numerous combinations of microstructures and constitutive laws are widely applied to match constitutive responses during the calibration process, which makes use of just a few parameters, owing to data scarcity. Friedman (1997) refers to these arbitraries as the "curse of dimensionality", in which calibrated DEM models are unable to provide accurate prediction [126–128]. Hanaor et al. (2013) developed specialized particle geometries for 3D printing by combining three different shape descriptors: fractal surface overlay, directed polyhedral aggregation, and contour rotation interpolation [129]. Thus, the discrete element method is implemented utilizing 3D printing technology. The method of contour rotation interpolation was determined to be the most appropriate, and synthetic particles were manufactured in bulk and submitted to triaxial testing. Three-dimensional geometries were employed to simulate triaxial testing using DEMs in order to compare them to experimental tests. The three-dimensional printed particles exhibited shear behavior and the effect of particle form on the bulk material responses. During the macro-mechanical research of particle behavior, the introduction of synthetic particles enabled the separation of particle shape and material characteristics. Currently, the printing resolution and commercially accessible printing materials limit the use of 3D printing for geotechnical testing. The bulk-printed granular materials are composed of irregular angular forms. Gupta et al. (2018) extracted particle geometries from micro-CT scans and utilized 3D printing to reproduce sand particles. The DEM simulations were performed using the particle morphologies acquired from micro-CT scans and compared to the use of shape descriptors in numerical modeling. Odometric experiments were conducted using the 3D-printed particles, and the findings were utilized to calibrate and validate the DEM models. Figure 28 shows typical preliminary DEM results. The direct shear test was simulated using sand particles in DEM and compared to the laboratory direct shear test result. The normal stress applied on the specimen was 100 kPa, and sphere particles were used to represent the sand particles in the simulation. From Figure 28, it can be seen that DEM is able to simulate the direct shear test, with an initial increase in shear stress until peak state is achieved and then a reduction to the residual state. However, there is a noticeable difference between the DEM simulation and

the laboratory test results. This difference is most likely due to the use of spheres instead of the actual sand particle shapes.

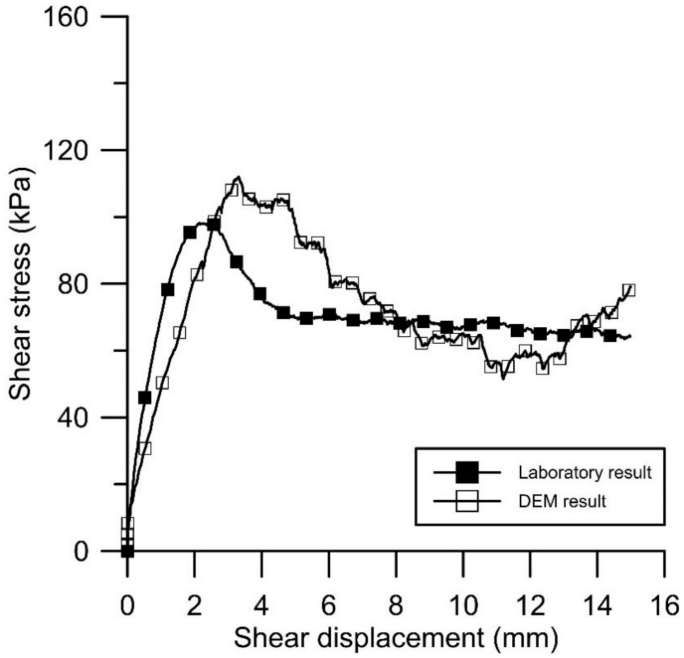


**Figure 28.** Typical DEM shear stress results compared against laboratory results for spheres or sphere clumps being used in DEM modeling.

Figure 29 shows state-of-the-art technologies being developed by the authors to improve the shear stress prediction of particles interacting with different material surfaces. The realistic particles obtained from micro-CT scanning can now be exported to DEM without the use of conventional spheres or sphere clumps. This technique is considered revolutionary at this stage of research. In this case, particle breakages can now be modeled in DEM to reflect the complex, true interparticle behavior. Hence, the proposed methodology of scanned particle shapes using micro-CT and printed particles for DEM calibration has much potential to contribute to more refined and accurate DEM results, which the authors will eventually publish. When sample extraction cannot be achieved due to site restrictions or unavailability of laboratory tests, the DEM technique will one day provide an extensive advantage to accurately model soil–structure interactions.

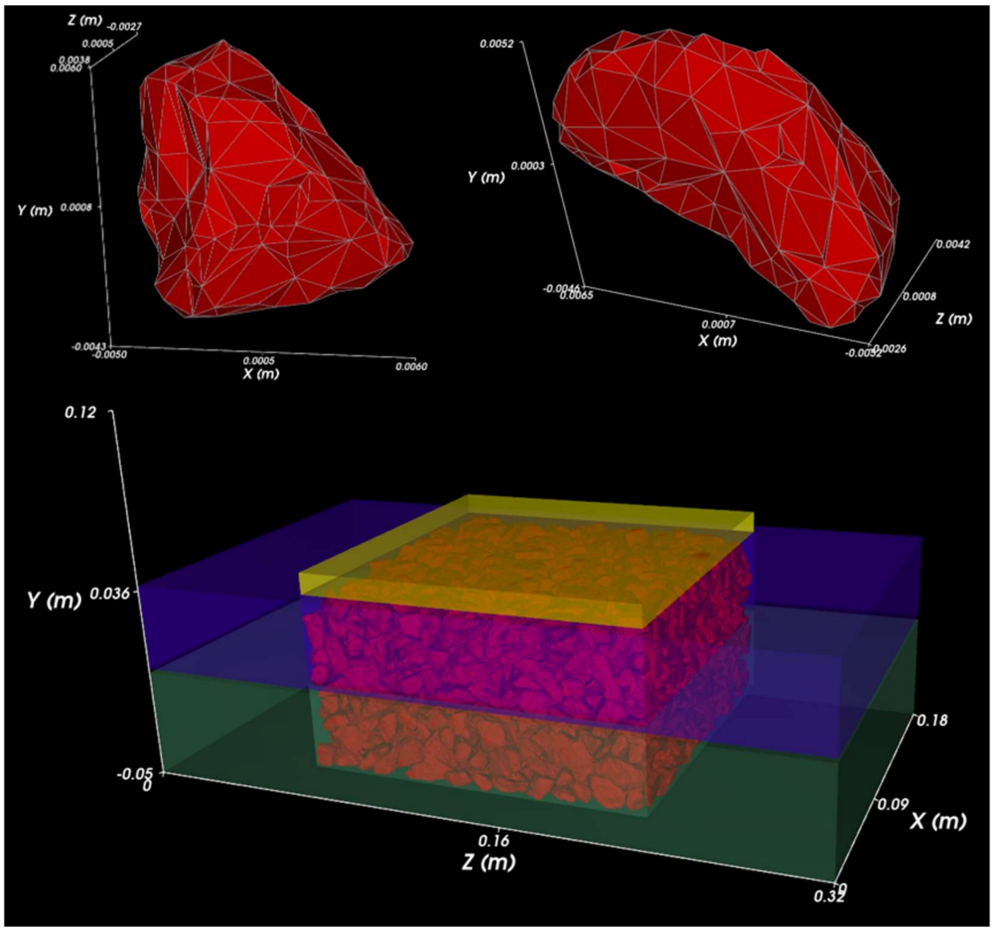


**Figure 29.** Realistic particle shapes are being used in DEM modeling as a revolutionary technique currently being developed by the authors.

### *5.3. Bayesian Method*

Bayesian method, a machine learning technique based on Bayes' theorem [130], is widely used due to its ability to quantify parameter uncertainty using probability. It computes the evolution of probability in the parameters, before observing the data, and after incorporating the data in the analysis [131]. It is found to be superior in updating, for example, soil parameters [132,133] or, in this case, surface roughness from prior studies, because it considers these parameters as random variables instead of fixed constants. Thus, the Bayesian updating process provides a robust approach in back analyzing or predicting soil parameters based on the field observational method compared to deterministic techniques that produce outputs with fixed values [134]. The probabilistic estimates obtained from a Bayesian model are used to quantify the parameter uncertainties to inform the confidence levels associated with the model predictions, thus making it a potentially suitable method to be applied to the study of interface surface roughness as a function of different soil types for the design of soil–structure interactions.

## 6. Conclusions and Recommendations

Interface shear mechanisms have been investigated through various shear tests and applied in geotechnical engineering applications. Previous research found that several influential factors affect the interface shear mechanism, such as (i) surface roughness, (ii) particle angularity, (iii) mean particle size, (iv) surface hardness, (v) particle breakage, and (vi) confinement condition. The main contributions of this review paper are in highlighting the following important observations:

- To parametrically study the interface shear mechanism, portable surface roughness gauges are required to evaluate surface roughness. For random or ribbed surface form, the maximum interface strength equals the soil strength, called "$\delta = \varnothing$ condition". For structured surface form, the shear strength of the interface shear test is not only developed by interfacial friction between the sand particle and structure surface as "$\delta = \varnothing$ condition", but additional passive resistance generated. Thus, the maximum interface strength is greater than the soil strength, called "$\delta > \varnothing$ condition".
- Particle angularity influences the friction development and mobilization of loads between soil–material interfaces. The increment in particle angularity leads to a more significant particle interlocking and higher peak shear strength.
- Mean particle size influences the interface shear mechanism corresponding to surface roughness and material texture.
- Surface hardness affects plowing behavior on the soil–material interface. The effective shear stress of the particle decreases until the contact area reaches the specific value. Once the normal stress reaches the limit state, an additional increment in normal stress causes particle movement and particle plowing, leading to shear stress increasing.
- The higher void ratios and poorer mineralogy of the particles resulted in anticipated particle breakages, significantly reducing the beneficial particle interlocking phenomena. Consequently, using flaky metagraywacke and shale particles as examples, a lack of interlocking activity results in decreased apparent cohesion, and thus a lower opportunity for strength development.
- The shearing boundaries (or limits) for soil specimens placed in the shear box vary with different shear apparatus set up. Moreover, the higher the normal stress, the more significant the particle interlocking and shear strength values would be. Thus, the selection of shear apparatus and normal stress range should match the real-life site conditions.

PIV technology is the main verification tool adopted in this paper to track and justify particle movements and interlocking during shear testing. According to the shear test results, interface shear strength is enhanced with the increment in surface roughness and gradually approaches the actual soil shear strength, when the material surface is in a random or ribbed form. Similarly, the increasing peak friction angle progressively approaches the soil internal friction angle until the surface roughness reaches its critical roughness. These observations prove that surface roughness has a negligible influence on residual friction angle. In parallel, the application of PIV technology demonstrates that the four-stage model is highly applicable and reliable to describe the development of soil shear strength in the direct shear tests and the interface shear tests. With the development of other advanced testing and verification methods (e.g., ANN, DEM, 3D printing, and Bayesian machine learning), the research of interface shear mechanisms is becoming more important and relevant in the study of soil–structure interactions. The conclusions and recommendations are presented below:

- Artificial neural network has the potential to establish a nonlinear relationship to investigate the mutual coupling effect of surface roughness and other factors on the interface shear mechanism.
- Rather than the spherical model that is frequently used in DEM, a micro-CT-scanned 3D model of the actual particle morphologies can be employed to enhance the simulation quality.
- In the calibration of interface shear tests, 3D printing of synthetic particles is recommended to validate the DEM results.
- Bayesian method considers soil and interface parameters as random variables and provides probabilistic estimates to reasonably quantify the parameter uncertainties and may be used in interface shear studies to develop a greater understanding in the study of soil–structure interactions.

**Author Contributions:** Conceptualization, R.W., D.E.L.O. and M.I.P.; methodology, R.W., D.E.L.O. and M.I.P.; software, R.W.; validation, R.W., D.E.L.O. and M.I.P.; formal analysis, R.W. and M.I.P.; investigation, R.W. and M.I.P.; resources, R.W., D.E.L.O., M.I.P. and D.-S.J.; data curation, R.W.; writing—original draft preparation, R.W. and D.E.L.O.; writing—review and editing, R.W., D.E.L.O., M.I.P. and D.-S.J.; visualization, R.W. and; supervision, D.E.L.O. and D.-S.J.; project administration, D.E.L.O. and D.-S.J.; funding acquisition, D.E.L.O. All authors have read and agreed to the published version of the manuscript.

**Funding:** This research received no external funding.

**Institutional Review Board Statement:** Not applicable.

**Informed Consent Statement:** Not applicable.

**Data Availability Statement:** The original experimental data are available on request from the corresponding author.

**Conflicts of Interest:** The authors declare no conflict of interest.

## References

1. Leong, H.Y.; Ong, D.E.L.; Sanjayan, J.G.; Nazari, A. A genetic programming predictive model for parametric study of factors affecting strength of geopolymers. *RSC Adv.* **2015**, *5*, 85630–85639. [CrossRef]
2. Leong, H.Y.; Ong, D.E.L.; Sanjayan, J.; Nazari, A. The effect of different $Na_2O$ and $K_2O$ ratios of alkali activator on compressive strength of fly ash based-geopolymer. *Constr. Build. Mater.* **2016**, *106*, 500–511. [CrossRef]
3. Leong, H.Y.; Ong, D.E.L.; Sanjayan, J.; Nazari, A. Suitability of Sarawak and Gladstone fly ash to produce geopolymers: A physical, chemical, mechanical, mineralogical and microstructural analysis. *Ceram. Int.* **2016**, *42*, 9613–9620. [CrossRef]
4. Ngu, L.; Song, J.W.; Hashim, S.S.; Ong, D.E. Lab-scale atmospheric $CO_2$ absorption for calcium carbonate precipitation in sand. *Greenh. Gases Sci. Technol.* **2019**, *9*, 519–528. [CrossRef]
5. Mehdizadeh, A.; Disfani, M.M.; Evans, R.; Arulrajah, A.; Ong, D.E.L. Discussion of "Development of an Internal Camera-Based Volume Determination System for Triaxial Testing" by S.E. Salazar, A. Barnes and R.A. Coffman. *Geotech. Test. J. 2015, 38; reprinted in Geotech. Test. J.* **2016**, *39*, 165–168. [CrossRef]
6. Mehdizadeh, A.; Disfani, M.M.; Evans, R.; Arulrajah, A.; Ong, D.E.L. Mechanical Consequences of Suffusion on Undrained Behaviour of a Gap-Graded Cohesionless Soil—An Experimental Approach. *Geotech. Test. J.* **2017**, *40*, 1026–1042. [CrossRef]
7. Ong, D.E.L. Benchmarking of FEM technique involving deep excavation, pile-soil interaction and embankment construction. In Proceedings of the 12th International Conference of International Association for Computer Methods and Advanced in Geomechanics (IACMAG), Goa, India, 1–6 October 2008.
8. Ong, D.E.L.; Yang, D.; Phang, S. Comparison of finite element modelling of a deep excavation using SAGECRISP and PLAXIS. In Proceedings of the 2006 International Conference on Deep Excavations, Singapore, 28–30 June 2006; pp. 50–63.
9. Omoregie, A.; Khoshdelnezamiha, G.; Senian, N.; Ong, D.E.L.; Nissom, P.M. Experimental optimisation of various cultural conditions on urease activity for isolated Sporosarcina pasteurii strains and evaluation of their biocement potentials. *Ecol. Eng.* **2017**, *109*, 65–75. [CrossRef]
10. Omoregie, A.I.; Ngu, L.H.; Ong, D.E.L.; Nissom, P.M. Low-cost cultivation of Sporosarcina pasteurii strain in food-grade yeast extract medium for microbially induced carbonate precipitation (MICP) application. *Biocatal. Agric. Biotechnol.* **2019**, *17*, 247–255. [CrossRef]
11. Omoregie, A.I.; Ong, D.E.L.; Nissom, P.M. Assessing ureolytic bacteria with calcifying abilities isolated from limestone caves for biocalcification. *Lett. Appl. Microbiol.* **2019**, *68*, 173–181. [CrossRef] [PubMed]
12. Omoregie, A.I.; Palombo, E.A.; Ong, D.E.; Nissom, P.M. Biocementation of sand by Sporosarcina pasteurii strain and technical-grade cementation reagents through surface percolation treatment method. *Constr. Build. Mater.* **2019**, *228*, 116828. [CrossRef]
13. Omoregie, A.I.; Palombo, E.A.; Ong, D.E.; Nissom, P.M. A feasible scale-up production of Sporosarcina pasteurii using custom-built stirred tank reactor for in-situ soil biocementation. *Biocatal. Agric. Biotechnol.* **2020**, *24*, 101544. [CrossRef]
14. Omoregie, A.I.; Senian, N.; Li, P.Y.; Hei, N.L.; Leong, D.O.E.; Ginjom, I.R.H.; Nissom, P.M. Ureolytic bacteria isolated from Sarawak limestone caves show high urease enzyme activity comparable to that of Sporosarcina pasteurii (DSM 33). *Malays. J. Microbiol.* **2016**, *12*, 463–470.
15. Leong, H.Y.; Ong, D.E.L.; Sanjayan, J.G.; Nazari, A. Strength Development of Soil–Fly Ash Geopolymer: Assessment of Soil, Fly Ash, Alkali Activators, and Water. *J. Mater. Civ. Eng.* **2018**, *30*, 04018171. [CrossRef]
16. Leong, H.Y.; Ong, D.E.L.; Sanjayan, J.G.; Nazari, A.; Kueh, S.M. Effects of Significant Variables on Compressive Strength of Soil-Fly Ash Geopolymer: Variable Analytical Approach Based on Neural Networks and Genetic Programming. *J. Mater. Civ. Eng.* **2018**, *30*, 04018129. [CrossRef]
17. Liu, Y.; Liu, Z.; Oh, E.; Ong, D. Strength and Microstructural Assessment of Reconstituted and Stabilised Soft Soils with Varying Silt Contents. *Geosciences* **2021**, *11*, 302. [CrossRef]

18. Chong, E.; Ong, D. Data-Driven Field Observational Method of a Contiguous Bored Pile Wall System Affected by Accidental Groundwater Drawdown. *Geosciences* **2020**, *10*, 268. [CrossRef]
19. Ong, D.E.L.; Choo, C. 2011, Sustainable construction of a bored pile foundation system in erratic phyllite. In Proceedings of the 2011 ASEAN-Australian Engineering Congress, Kuching, Malaysia, 25–27 July 2011; pp. 50–65.
20. Ong, D.E.L.; Leung, C.; Chow, Y. Piles subject to excavation-induced soil movement in clay. In Proceedings of the 13th European Conference on Soil Mechanics and Geotechnical Engineering, Prague, Czech Republic, 25–28 August 2003; pp. 777–782.
21. Ong, D.E.L.; Leung, C.; Chow, Y. Time-dependent Pile Behavior due to Excavation-Induced Soil Movement in Clay. In Proceedings of the 12th Pan-American Conference on Soil Mechanics and Geotechnical Engineering, Cambridge, MA, USA, 22–26 June 2003; Massachusetts Institute of Technology: Boston, MA, USA, 2003; Volume 2, pp. 2035–2040.
22. Ong, D.E.L.; Leung, C.F.; Chow, Y.K.; Ng, T.G. Severe Damage of a Pile Group due to Slope Failure. *J. Geotech. Geoenviron. Eng.* **2015**, *141*, 04015014. [CrossRef]
23. Ong, D.E.L.; Sim, Y.S.; Leung, C.F. Performance of Field and Numerical Back-Analysis of Floating Stone Columns in Soft Clay Considering the Influence of Dilatancy. *Int. J. Géoméch.* **2018**, *18*, 04018135. [CrossRef]
24. Liu, Z.; Ong, D.E.L.; Liu, Y.; Bolton, M.W.; Oh, E. Effect of Cement and Bentonite Mixture on the Consolidation Behavior of Soft Estuarine Soils. *Int. J. GEOMATE* **2020**, *18*, 49–54. [CrossRef]
25. Sun, J.; Oh, E.; Ong, D. Influence of Degree of Saturation (DOS) on Dynamic Behavior of Unbound Granular Materials. *Geosciences* **2021**, *11*, 89. [CrossRef]
26. Cheng, W.-C.; Li, G.; Ong, D.E. Lubrication characteristics of pipejacking in soft alluvial deposits. In *Geotechnical Aspects of Underground Construction in Soft Ground*; CRC Press: Boca Raton, FL, USA, 2021; pp. 12–18. [CrossRef]
27. Cheng, W.-C.; Li, G.; Ong, D.E.; Chen, S.-L.; Ni, J.C. Modelling liner forces response to very close-proximity tunnelling in soft alluvial deposits. *Tunn. Undergr. Space Technol.* **2020**, *103*, 103455. [CrossRef]
28. Peerun, M.I.; Ong, D.E.L.; Choo, C.S. Calibration and parametric studies using geopiv technology to track particle movements in a transparent shear box. In Proceedings of the Young Geotechnical Engineers Conference 2016: Contributions of Young Geotechnical Engineers to Nation Building, Petaling Jaya, Selangor, Malaysia, 30 May 2016. [CrossRef]
29. Peerun, M.I.; Ong, D.E.L.; Choo, C.S. Interpretation of Geomaterial Behavior during Shearing Aided by PIV Technology. *J. Mater. Civ. Eng.* **2019**, *31*, 04019195. [CrossRef]
30. Peerun, M.; Ong, D.; Choo, C.; Cheng, W. Effect of interparticle behavior on the development of soil arching in soil-structure interaction. *Tunn. Undergr. Space Technol.* **2020**, *106*, 103610. [CrossRef]
31. Peerun, M.I.; Ong, D.E.L.; Desha, C.; Oh, E.; Choo, C. Influences of geological characteristics on the construction of tunnels. In Proceedings of the WEC2019: World Engineers Convention 2019, Melbourne, VIC, Australia, 20–22 November 2019.
32. Ong, D.E.L. Pile Behaviour Subject to Excavation-Induced Soil Movement in Clay. Ph.D. Thesis, National University of Singapore, Singapore, 2005.
33. Peerun, M.I.; Ong, D.E.L.; Choo, C.S.; Phangkawira, F. *Novel Methods in Estimating Pipe-Jacking Forces in Highly Fractured Rocks*; Indian Society for Trenchless Technology, NoDIG: Delhi, India, 2017.
34. Kang, G.; Tsuchida, T.; Athapaththu, A. Strength mobilization of cement-treated dredged clay during the early stages of curing. *Soils Found.* **2015**, *55*, 375–392. [CrossRef]
35. Liu, Y.; Jiang, Y.J.; Xiao, H.; Lee, F.H. Determination of representative strength of deep cement-mixed clay from core strength data. *Géotechnique* **2017**, *67*, 350–364. [CrossRef]
36. Yao, K.; Pan, Y.; Jia, L.; Yi, J.T.; Hu, J.; Wu, C. Strength evaluation of marine clay stabilized by cementitious binder. *Mar. Georesour. Geotechnol.* **2020**, *38*, 730–743. [CrossRef]
37. Zhou, J. Performance of Full Scale Tests of Piles in Different Soil Conditions. Ph.D. Thesis, Griffith University, Brisbane, Australia, 2018.
38. Zhou, J.; Zhang, X.; Zhang, L.; Dong, F.; Oh, E. Static load tests of driven concrete piles under CFRP confinement. *Géoméch. Geoengin.* **2020**, *15*, 159–171. [CrossRef]
39. Cheng, W.-C.; Ni, J.C.; Huang, H.-W.; Shen, J.S. The use of tunnelling parameters and spoil characteristics to assess soil types: A case study from alluvial deposits at a pipejacking project site. *Bull. Eng. Geol. Environ.* **2019**, *78*, 2933–2942. [CrossRef]
40. Ji, X.; Zhao, W.; Ni, P.; Barla, M.; Han, J.; Jia, P.; Chen, Y.; Zhang, C. A method to estimate the jacking force for pipe jacking in sandy soils. *Tunn. Undergr. Space Technol.* **2019**, *90*, 119–130. [CrossRef]
41. Coulomb, C. Sur une Application des Regles de Mximus et Mnimus a Qelques Poblemes de Satique Rlatits a L'architecture, Academie Royale des Sciences. In *Memoires de Mathermatiques et de Physique par Divers Sowans*; Academy of Sciences: Paris, France, 1773; Volume 7, pp. 343–382.
42. Staheli, K. Jacking Force Prediction: An Interface Friction Approach Based on Pipe Surface Roughness. Ph.D. Thesis, Georgia Institute of Technology, Atlanta, GA, USA, 2006.
43. Paikowsky, S.; Player, C.; Connors, P. A Dual Interface Apparatus for Testing Unrestricted Friction of Soil Along Solid Surfaces. *Geotech. Test. J.* **1995**, *18*, 168–193. [CrossRef]
44. Uesugi, M.; Kishida, H. Frictional Resistance at Yield between Dry Sand and Mild Steel. *Soils Found.* **1986**, *26*, 139–149. [CrossRef]
45. Frost, J.; DeJong, J.; Recalde, M. Shear failure behavior of granular–continuum interfaces. *Eng. Fract. Mech.* **2002**, *69*, 2029–2048. [CrossRef]

46. Edil, T.B.; Bosscher, P.J.; Sundberg, A.J. Soil-Structure Interface Shear Transfer Behavior. In *Geomechanics II: Testing, Modeling, and Simulation*; Springer: Berlin/Heidelberg, Germany, 2006; pp. 528–543. [CrossRef]
47. Uesugi, M.; Kishida, H. Influential Factors of Friction between Steel and Dry Sands. *Soils Found.* **1986**, *26*, 33–46. [CrossRef]
48. Jardine, R.J.; Lehane, B.M.; Everton, S.J. Friction Coefficients for Piles in Sands and Silts. In *Offshore Site Investigation and Foundation Behaviour. Advances in Underwater Technology, Ocean Science and Offshore Engineering*; Ardus, D.A., Clare, D., Hill, A., Hobbs, R., Jardine, R.J., Squire, J.M., Eds.; Springer: Dordrecht, The Netherlands, 1993; Volume 28, pp. 661–677. [CrossRef]
49. Ho, T.; Jardine, R.; Anh-Minh, N. Large-displacement interface shear between steel and granular media. *Géotechnique* **2011**, *61*, 221–234. [CrossRef]
50. Boulon, M. Physical and numerical simulation of lateral shaft friction along offshore piles in sand. In Proceedings of the 3rd Internation Conference on Numerical Methods in Offshore Piling, Paris, France; 1986; pp. 127–147. [CrossRef]
51. Dove, J.E.; Frost, J.D. Peak Friction Behavior of Smooth Geomembrane-Particle Interfaces. *J. Geotech. Geoenviron. Eng.* **1999**, *125*, 544–555. [CrossRef]
52. Peerun, I.; Ong, D.; Choo, C. Behaviour of reconstituted sand-sized particles in direct shear tests using PIV technology. *Jpn. Geotech. Soc. Spéc. Publ.* **2016**, *2*, 354–359. [CrossRef]
53. Peerun, M.I.; Ong, D.E.L.; Choo, C.S. Effect of Particle Shapes on Shear Strength during Direct Shear Testing using GeoPIV Technology. In Proceedings of the 19th Southeast Asian Geotechnical Conference & 2nd Agssea Conference, Deep Excavation and Ground Improvement Dorsett Grand Subang, Subang Jaya, Malaysia, 31 May–3 June 2016.
54. Pellet-Beaucour, A.-L.; Kastner, R. Experimental and analytical study of friction forces during microtunneling operations. *Tunn. Undergr. Space Technol.* **2002**, *17*, 83–97. [CrossRef]
55. Samtani, N.C.; Nowatzki, E.A. *Soils and Foundations: Reference Manual–Volume I, Report, United States*; Federal Highway Administration: Washington, DC, USA, 2006.
56. *AS1289*; Methods of Testing Soils for Engineering Purposes. Standards Association of Australia: Sydney, NSW, Australia, 1998.
57. *GB/T50123*; Geotechnical Test Method Standard. China Planning Press: Beijing, China, 1999. (In Chinese)
58. *ASTM, D3080*; Standard Test Method for Direct Shear Test of Soils Under Consolidated Drained Conditions. ASTM International: West Conshohocken, PA, USA, 2004.
59. Yu, K.; Yao, X.; Zhang, Y.; Li, C.; Ou, L. Analysis of direct shear test data based on area and stress correction. *Chin. J. Rock Mech. Eng.* **2014**, *33*, 118–124. (In Chinese)
60. Li, Y.; Aydin, A. Behavior of rounded granular materials in direct shear: Mechanisms and quantification of fluctuations. *Eng. Geol.* **2010**, *115*, 96–104. [CrossRef]
61. Bjerrum, L.; Landva, A. Direct Simple-Shear Tests on a Norwegian Quick Clay. *Géotechnique.* **1966**, *16*, 1–20. [CrossRef]
62. Shimamura, A.; Miyamoto, Y.; Kobayashi, T. Experimental Study on Lateral Resistance of Steel Pipe Pile with Wings Using the New Composite Geo-material with Magnesium Acrylate. In *Dynamic Soil-Structure Interaction for Sustainable Infrastructures. GeoMEast 2018. Sustainable Civil Infrastructures*; Choudhury, D., El-Zahaby, K., Idriss, I., Eds.; Springer: Cham, Switzerland, 2018; pp. 62–74. [CrossRef]
63. Hanzawa, H.; Nutt, N.; Lunne, T.; Tang, Y.; Long, M. A Comparative Study Between the NGI Direct Simple Shear Apparatus and the Mikasa Direct Shear Apparatus. *Soils Found.* **2007**, *47*, 47–58. [CrossRef]
64. *ASTM, D6528*; Standard Test Method for Consolidated Undrained Direct Simple Shear Testing of Fine Grain Soils. ASTM International: West Conshohocken, PA, USA, 2017.
65. Bishop, A.W.; Green, G.E.; Garga, V.K.; Andresen, A.; Brown, J.D. A New Ring Shear Apparatus and Its Application to the Measurement of Residual Strength. *Géotechnique* **1971**, *21*, 273–328. [CrossRef]
66. Bromhead, E.N.; Dixon, N. The field residual strength of London Clay and its correlation with loboratory measurements, especially ring shear tests. *Géotechnique* **1986**, *36*, 449–452. [CrossRef]
67. Stark, T.D.; Eid, H.T. Modified Bromhead ring shear apparatus. *Geotech. Test. J.* **1993**, *16*, 100–107. [CrossRef]
68. Varnes, D.J. Slope movement types and processes. In *Transportation Research Board, Special Report*; Transportation Research Board: Washington, DC, USA, 1978; Volume 176, pp. 11–33.
69. Peerun, M.I. Behaviour of Reconstituted Sand-Sized Tunnelling Rock Spoils during Shearing Using GeoPIV Technology for the Assessment of Soil Arching Effect during Pipe-Jacking Works. Master's Thesis, Faculty of Engineering, Computing and Science, Swinburne University of Technology, Hawthorn, VIC, Australia, 2016.
70. Keramatikerman, M.; Chegenizadeh, A.; Nikraz, H.; Yilmaz, Y. Mechanical Behaviour of Atrazine-Contaminated Clay. *Appl. Sci.* **2020**, *10*, 2457. [CrossRef]
71. Potyondy, J.G. Skin Friction between Various Soils and Construction Materials. *Géotechnique* **1961**, *11*, 339–353. [CrossRef]
72. *ISO 4278:1977*; Geometrical Product Specifications (GPS)—Surface Texture: Profile Method—Terms, Definitions and Surface Texture Parameters. International Organization for Standardization: Geneva, Switzerland, 1977.
73. Rudawska, A.; Danczak, I.; Müller, M.; Valasek, P. The effect of sandblasting on surface properties for adhesion. *Int. J. Adhes. Adhes.* **2016**, *70*, 176–190. [CrossRef]
74. Yoshimi, Y.; Kishida, T. A Ring Torsion Apparatus for Evaluating Friction Between Soil and Metal Surfaces. *Geotech. Test. J.* **1981**, *4*, 145–152. [CrossRef]
75. Kishida, H.; Uesugi, M. Tests of the interface between sand and steel in the simple shear apparatus. *Géotechnique* **1987**, *37*, 45–52. [CrossRef]

76. Subba Rao, K.; Allam, M.; Robinson, R.; Paikowsky, S.; Player, C. Discussion on a dual interface apparatus for testing unrestricted friction of soil along solid surfaces. Authors' reply. *ASTM Geotech. Test. J.* **1996**, *19*, 446–451. [CrossRef]
77. Zhou, X.; Gong, W.; Ding, H.; Rao, X. Large-scale simple shear test on mechanical properties of interface between concrete face and gravel underlayer. *Chin. J. Geotech. Eng.* **2005**, *27*, 876–880.
78. Iscimen, M.; Frost, J. Shearing behaviour of curved interfaces. In *Characterization and Behavior of Interfaces: Proceedings of the Research Symposium on Characterization and Behavior of Interfaces, Atlanta, GA, USA, 21 September 2008*; IOS Press: Amsterdam, The Netherlands, 2010; pp. 35–43.
79. Knappett, J.; Craig, R.F. *Craig's Soil Mechanics*, 9th ed.; CRC Press: London, UK, 2019; Volume 8. [CrossRef]
80. Stępień, K. Testing the Accuracy of Surface Roughness Measurements Carried out with a Portable Profilometer. *Key Eng. Mater.* **2015**, *637*, 69–73. [CrossRef]
81. Mell, B. *Sandpaper Roughness Measurement Using 3D Profilometry*; Nanovea Technical Report; Nanovea: Irvine, CA, USA, 2010.
82. Liu, F. *Roughness and Particle Diameter of Sandpaper*; Nanovea Technical Report; Nanovea: Irvine, CA, USA, 2018.
83. Martinez, A.; Frost, J.D. The influence of surface roughness form on the strength of sand-structure interfaces. *Géotechnique Lett.* **2017**, *7*, 104–111. [CrossRef]
84. Tsubakihara, Y.; Kishida, H. Frictional Behaviour between Normally Consolidated Clay and Steel by Two Direct Shear Type Apparatuses. *Soils Found.* **1993**, *33*, 1–13. [CrossRef]
85. Chen, X.; Zhang, J.; Xiao, Y.; Li, J. Effect of roughness on shear behavior of red clay—Concrete interface in large-scale direct shear tests. *Can. Geotech. J.* **2015**, *52*, 1122–1135. [CrossRef]
86. Hryciw, R.D.; Irsyam, M. Behavior of Sand Particles Around Rigid Ribbed Inclusions During Shear. *Soils Found.* **1993**, *33*, 1–13. [CrossRef]
87. Koval, G.; Chevoir, F.; Roux, J.-N.; Sulem, J.; Corfdir, A. Interface roughness effect on slow cyclic annular shear of granular materials. *Granul. Matter* **2011**, *13*, 525–540. [CrossRef]
88. Mitchell, J.K.; Villet, W.C. *Reinforcement of Earth Slopes and Embankments*; NCHRP Report; Transportation Research Board: Washington, DC, USA, 1987.
89. Dyskin, A.V.; Estrin, Y.; Kanel-Belov, A.; Pasternak, E. Toughening by Fragmentation—How Topology Helps. *Adv. Eng. Mater.* **2001**, *3*, 885–888. [CrossRef]
90. Miura, K.; Maeda, K.; Furukawa, M.; Toki, S. Mechanical Characteristics of Sands with Different Primary Properties. *Soils Found.* **1998**, *38*, 159–172. [CrossRef]
91. Shimobe, S.; Moroto, N. A new classification chart for sand liquefaction. *Earthq. Geotech. Eng.* **1995**, 315–320.
92. Cho, G.-C.; Dodds, J.; Santamarina, J.C. Closure to "Particle Shape Effects on Packing Density, Stiffness, and Strength: Natural and Crushed Sands" by Gye-Chun Cho, Jake Dodds, and J. Carlos Santamarina. *J. Geotech. Geoenvironmental Eng.* **2007**, *133*, 1474. [CrossRef]
93. *ASTM, D2488-17*; Standard Practice for Description and Identification of Soils (Visual-Manual Procedure). ASTM International: West Conshohocken, PA, USA, 2017. [CrossRef]
94. De Graft-Johnson, J.; Bhatia, H.; Gidigasu, D. The strength characteristics of residual micaceous soils and their application to stability problems. In Proceedings of the 7th International Conference on Soil Mechanics and Foundation Engineering, Mexico City, Maxico; 1969; Volume 2.
95. Holtz, W.; Willard, M. *Triaxial Shear Characteristics of Clayey Gravel Soils*; US Bureau of Reclamation: Washington, DC, USA, 1961.
96. Choo, C.S.; Ong, D.E.L. Evaluation of Pipe-Jacking Forces Based on Direct Shear Testing of Reconstituted Tunneling Rock Spoils. *J. Geotech. Geoenviron. Eng.* **2015**, *141*, 04015044. [CrossRef]
97. Ong, D.; Choo, C. Assessment of non-linear rock strength parameters for the estimation of pipe-jacking forces. Part 1. Direct shear testing and backanalysis. *Eng. Geol.* **2018**, *244*, 159–172. [CrossRef]
98. Vangla, P.; Gali, M.L. Effect of particle size of sand and surface asperities of reinforcement on their interface shear behaviour. *Geotext. Geomembr.* **2016**, *44*, 254–268. [CrossRef]
99. Punetha, P.; Mohanty, P.; Samanta, M. Microstructural investigation on mechanical behavior of soil-geosynthetic interface in direct shear test. *Geotext. Geomembr.* **2017**, *45*, 197–210. [CrossRef]
100. Su, L.-J.; Zhou, W.-H.; Chen, W.-B.; Jie, X. Effects of relative roughness and mean particle size on the shear strength of sand-steel interface. *Measurement* **2018**, *122*, 339–346. [CrossRef]
101. Williams, J.A.; Kennedy, F.E. Engineering Tribology. *ASME J. Tribol.* **1998**, *120*, 644. [CrossRef]
102. Xiao, Y.; Liu, H.; Chen, Y.; Jiang, J. Strength and Deformation of Rockfill Material Based on Large-Scale Triaxial Compression Tests. I: Influences of Density and Pressure. *J. Geotech. Geoenviron. Eng.* **2014**, *140*, 04014070. [CrossRef]
103. Terzaghi, K.; Peck, R.B.; Mesri, G. *Soil Mechanics in Engineering Practice*; John Wiley & Sons: Hoboken, NJ, USA, 1996.
104. Adrian, R.J. Particle-Imaging Techniques for Experimental Fluid Mechanics. *Annu. Rev. Fluid Mech.* **1991**, *23*, 261–304. [CrossRef]
105. Grant, I. Particle image velocimetry: A review. *Proc. Inst. Mech. Eng. Part C J. Mech. Eng. Sci.* **1997**, *211*, 55–76. [CrossRef]
106. White, D.; Take, W. *GeoPIV: Particle Image Velocimetry (PIV) Software for Use in Geotechnical Testing*; Cambridge University: Cambridge, UK, 2002.
107. Ng, N.Y.J.; Peerun, M.I.; Ong, D.E.L.; Choo, C.S. *Assessment of Tunnelling Rock Spoils from Highly Weathered Lithology Using Rolling Friction Contact Models in Discrete Element Modelling*; The Institution of Engineers Malaysia: Kuala Lumpur, Malaysia, 2020.

108. Peerun, M.I.; Ong, D.E.L.; Desha, C.; Oh, E.; Choo, C.S. Advances in the Study of Micromechanical Behaviour for Granular Materials Using Micro-CT Scanner and 3D Printing. In *Challenges and Innovations in Geomechanics*; IACMAG 2021. Lecture Notes in Civil Engineering; Barla, M., Di Donna, A., Sterpi, D., Eds.; Springer: Cham, Switzerland, 2021; Volume 125, pp. 911–918. [CrossRef]
109. Peerun, M.I.; Ong, D.E.L.; Desha, C.; Oh, E.; Choo, C.S. Recent Advancements in Fundamental Studies of Particulate Interaction and Mechanical Behaviour using 3-D Printed Synthetic Particles. In Proceedings of the 1st Malaysian Geotechincal Society (MGS) and Geotechnical Society of Singapore (GeoSS) Conference 2019, Petaling Jaya, Malaysia, 24–26 June 2019.
110. Indraratna, B.; Ngo, T.; Rujikiatkamjorn, C.; Vinod, J.S. Behavior of Fresh and Fouled Railway Ballast Subjected to Direct Shear Testing: Discrete Element Simulation. *Int. J. Géoméch.* **2014**, *14*, 34–44. [CrossRef]
111. Potts, D.M.; Dounias, G.T.; Vaughan, P.R. Finite element analysis of the direct shear box test. *Géotechnique* **1987**, *37*, 11–23. [CrossRef]
112. Fukuoka, H.; Sassa, K.; Wang, G.; Sasaki, R. Observation of shear zone development in ring-shear apparatus with a transparent shear box. *Landslides* **2006**, *3*, 239. [CrossRef]
113. Agung, M.W.; Sassa, K.; Fukuoka, H.; Wang, G. Evolution of Shear-Zone Structure in Undrained Ring-Shear Tests. *Landslides* **2004**, *1*, 101–112. [CrossRef]
114. Wang, G.; Sassa, K. Post-failure mobility of saturated sands in undrained load-controlled ring shear tests. *Can. Geotech. J.* **2002**, *39*, 821–837. [CrossRef]
115. Yuan, Q.; Wang, Y.H.; Tam, P.O.; Li, X.; Gao, Y. Experimental Characterizations of Contact Movement in Two-Dimensional Rod Assembly Subjected to Direct Shearing. *Int. J. Géoméch.* **2017**, *17*, 04016032. [CrossRef]
116. Choo, C.S.; Ong, D.E.L. Impact of highly weathered geology on pipe-jacking forces. *Geotech. Res.* **2017**, *4*, 94–106. [CrossRef]
117. Ong, D.E.L.; Choo, C.S. Back-analysis and finite element modeling of jacking forces in weathered rocks. *Tunn. Undergr. Space Technol.* **2016**, *51*, 1–10. [CrossRef]
118. Jewell, R.A. Direct shear tests on sand. *Géotechnique* **1989**, *39*, 309–322. [CrossRef]
119. Shahin, M.; Maier, H.; Jaksa, M. Predicting Settlement of Shallow Foundations using Neural Networks. *J. Geotech. Geoenvironmental Eng.* **2002**, *128*, 785–793. [CrossRef]
120. Fatehnia, M.; Amirinia, G. A review of Genetic Programming and Artificial Neural Network applications in pile foundations. *Int. J. Geo-Eng.* **2018**, *9*, 2. [CrossRef]
121. Fausett, L. *Fundamentals of Neural Networks: Architectures, Algorithms, and Applications*; Prentice-Hall, Inc.: Hoboken, NJ, USA, 1994.
122. Maier, H.; Dandy, G. The effect of internal parameters and geometry on the performance of back-propagation neural networks: An empirical study. *Environ. Model. Softw.* **1998**, *13*, 193–209. [CrossRef]
123. Ecemis, N.; Bakunowicz, P. Feasible packing of granular materials in discrete-element modelling of cone-penetration testing. *Géoméch. Geoeng.* **2018**, *13*, 198–216. [CrossRef]
124. Liu, Y.; Sun, W.; Fish, J. Determining Material Parameters for Critical State Plasticity Models Based on Multilevel Extended Digital Database. *J. Appl. Mech.* **2016**, *83*, 011003. [CrossRef]
125. Ng, T.-T. Input Parameters of Discrete Element Methods. *J. Eng. Mech.* **2006**, *132*, 723–729. [CrossRef]
126. Friedman, J.H. On bias, variance, 0/1—Loss, and the curse-of-dimensionality. *Data Min. Knowl. Discov.* **1997**, *1*, 55–77. [CrossRef]
127. Gupta, R.; Salager, S.; Wang, K.; Sun, W. Open-source support toward validating and falsifying discrete mechanics models using synthetic granular materials—Part I: Experimental tests with particles manufactured by a 3D printer. *Acta Geotech.* **2019**, *14*, 923–937. [CrossRef]
128. Wang, K.; Sun, W.; Salager, S.; Na, S.; Khaddour, G. Identifying Material Parameters for a Micro-Polar Plasticity Model via X-ray Micro-Computed Tomographic (ct) Images: Lessons Learned from the Curve-Fitting Exercises. *Int. J. Multiscale Comput. Eng.* **2016**, *14*, 389–413. [CrossRef]
129. Hanaor, D.A.H.; Gan, Y.; Einav, I. Effects of surface structure deformation on static friction at fractal interfaces. *Géotechnique Lett.* **2013**, *3*, 52–58. [CrossRef]
130. Bayes, T. LII. An essay towards solving a problem in the doctrine of chances. By the late Rev. Mr. Bayes, F.R.S. communicated by Mr. Price, in a letter to John Canton, A.M.F.R.S. *Philos. Trans. R. Soc. Lond.* **1763**, *53*, 370–418. [CrossRef]
131. Jin, Y.; Biscontin, G.; Gardoni, P. A Bayesian definition of 'most probable' parameters. *Geotech. Res.* **2018**, *5*, 130–142. [CrossRef]
132. Jong, S.; Ong, D.; Oh, E. State-of-the-art review of geotechnical-driven artificial intelligence techniques in underground soil-structure interaction. *Tunn. Undergr. Space Technol.* **2021**, *113*, 103946. [CrossRef]
133. Jong, S.C.; Ong, D.E.L.; Oh, E.; Choo, C.S. Prediction of Frictional Jacking Forces Using Bayesian Inference. In *Challenges and Innovations in Geomechanics*; Barla, M., Di Donna, A., Sterpi, D., Eds.; IACMAG 2021. Lecture Notes in Civil Engineering; Springer: Cham, Switzerland, 2021; Volume 125, pp. 878–885. [CrossRef]
134. Qi, X.-H.; Zhou, W.-H. An efficient probabilistic back-analysis method for braced excavations using wall deflection data at multiple points. *Comput. Geotech.* **2017**, *85*, 186–198. [CrossRef]